Computation of swirling hydromagnetic nanofluid flow containing gyrotactic microorganisms from a spinning disk to a porous medium with hall current and anisotropic slip effects.

UMAVATHI, J.C., BÉG, O.A., KHAN, U.F., BÉG, T.A. and KADIR, A.

2023

ZAMM - JOURNAL OF APPLIED MATHEMATICS AND MECHANICS

https://onlinelibrary.wiley.com/journal/15214001

Impact factor:1.603

Accepted March 3rd 2023

COMPUTATION OF SWIRLING HYDROMAGNETIC NANOFLUID FLOW CONTAINING GYROTACTIC MICROORGANISMS FROM A SPINNING DISK TO A POROUS MEDIUM WITH HALL CURRENT AND ANISOTROPIC SLIP EFFECTS

J. C. Umavathi[1*], O. Anwar Bég[2], Umar F. Khan[3], Tasveer A. Bég[4] and Ali Kadir[2]

[1]*Department of Mathematics, Gulbarga University, Gulbarga-585 106, Karnataka, INDIA.*

[2]*Multi-Physical Engineering Sciences Group, Aeronautical/Mechanical Engineering, Salford University, School of Science, Engineering and Environment (SEE), Newton Building, Manchester, M54WT, UK.*

[3]*Magnetic Materials, School of Engineering, Robert Gordon University, Garthdee Road, Aberdeen AB10 7GE, SCOTLAND.*

[4]*Engineering Mechanics Research, Israfil House, Dickenson Rd., Manchester, M13, UK.*

**Corresponding author- email: drumavathi@rediffmail.com*

ABSTRACT

Prompted by the advancements in hybrid bio-nano-swirling magnetic bioreactors, a mathematical model for the swirling flow from a rotating disk bioreactor to a magnetic fluid saturating a porous matrix and containing nanoparticles and gyrotactic micro-organisms has been developed. An axial magnetic field is administered which is perpendicular to the disk and Hall currents are included. The disk is assumed to be impervious and stretches in the radial direction with a power-law velocity. The Buongiorno nanoscale, Kuznetsov bioconvection and Darcy porous media models are deployed. Anisotropic momentum, thermal, nanoparticle concentration and motile micro-organism slip effects are incorporated. Stefan blowing is also simulated. The governing conservation equations are transformed with appropriate variables to a ordinary nonlinear differential equations. MATLAB bvp4c shooting quadrature is used to solve the emerging nonlinear, coupled ordinary differential boundary value problem under transformed boundary conditions. Verification with earlier solutions for the non-magnetic Von Karman bioconvection nanofluid case is conducted. Further validation of the general magnetic model is conducted with the Adomian decomposition method (ADM). Extensive visualization of velocity, temperature, nanoparticle concentration and motile microorganism density number profiles is presented for the impact of various parameters including magnetic interaction parameter, Hall current parameter, Darcy number, momentum slip, thermal slip, nanoparticle slip and microorganism slip. Computations are also performed for skin friction, Nusselt number, Sherwood number and motile micro-organism density number gradient. The simulations provide a useful benchmark for further studies.

KEYWORDS: *Magnetic nanofluids; Gyrotactic bioconvection; Von Karman swirling nano-bioreactor; Darcy law; Hall current; Axial magnetic field; Sherwood number; Micro-organism density number; MATLAB; ADM.*

1.INTRODUCTION

Modern engineering technologies are increasingly embracing biological phenomena to improve efficiency and increase sustainability. Micro-organisms offer some excellent advantages for

fuel cells, bioreactors and other systems. Nanotechnology has also emerged as a prominent area in the 21st century and has provided exciting new materials for enhancing engineering devices including electromagnetic nanofluids. Under certain circumstances the Navier-Stokes partial differential equations for viscous Newtonian fluids can be reduced to much simpler ordinary differential systems facilitating both analytical and numerical solutions. These flows are usually steady in nature and include Blasius boundary layer flow, Hiemenz stagnation flow and Von Kármán swirling flow. The latter is generated by a uniformly spinning infinitely long plane disk and was first considered in a monumental study by the great German engineer, Von Kármán [1] a century ago. In the proximity of the disk the fluid is rotated via friction which generates centrifugal forces resulting in the displacement of fluid radially outwards. Von Kármán swirling flows continue to be studied owing to their extensive applications in coating flows, turbine cooling, rotating combustors and medicine, and many excellent references are documented in Schlichting and Gersten [2]. Many extensions to the Von Karman problem have also been addressed including viscoelastic flows [3, 4], extended families of solutions [5], viscoplastic flows [6] and unsteady flows with wall transpiration [7].

In the 21st century there is a growing thrust to achieve ecologically sustainable designs in technology, many of which exploit biological mechanisms. Numerous different approaches have been explored including biomimetic materials, peristaltic pumps, ciliated channels and the use of micro-organisms [8]. Bioconvection relates to the propulsion of swimming micro-organisms, controlled by the response to a particular stimulus (taxis). Excellent appraisals of the hydrodynamic modelling of micro-organism propulsion have been given by Kessler [9] and Plesset *et al.* [10]. Many different types of taxes exist including gyrotaxis (controlled by torque) [11], phototaxis (light) [12], chemotaxis (chemical concentration e.g. oxygen) [13], geotaxis (gravity-driven) [14, 15] and others e.g. magneto-taxis and combinations [16]. The mathematical models developed for bioconvecting micro-organisms mimic the general behavior of independent individual micro-organisms and apply to both short-term movements of freely motile individuals (unicellular and multicellular), and longer-term orientation. The bacterial micro-organisms responding to these taxes can be manipulated to swim towards or away from a particular stimulus. For example, chemo-tactic bacteria may be compelled to swim towards or away from a chemical concentration gradient and magneto-tactic bacteria swim along magnetic field lines. Engineers are increasingly exploring the use of bioconvection in such devices [17, 18] which feature Von Karman swirling flow. The objective is to achieve green designs which are environmentally friendly [19-26]. Chlorella vulgaris microalgae are an example of gyrotactic bioconvecting micro-organisms that can achieve improved efficiency in such devices. In swirling flows of bioreactors, the rapid transport of cells is achieved. This achieves the desired improvements [26]. In the above studies electromagnetic effects have been neglected. However increasingly smart technologies in engineering are deploying

intelligent fluids which respond to external electrical or magnetic fields, or both. MHD [27] is the science of the synergy of electrically conducting fluent media and external magnetic fields. Mathematical models are developed in MHD by combining the Maxwell electromagnetic field equations with the Navier-Stokes viscous flow equations. Many different effects can then be simulated in magnetohydrodynamic flows including the transverse Lorentz magnetic body force, Ohmic dissipation (Joule heating), inclined (oblique) magnetic fields, magnetic induction, ion slip and Hall current effects. These phenomena can also be exploited in medical engineering applications which include cardiovascular flow control [28], MHD based biomedical micro-pumps, micro-bio-mixers, blood cell manipulation (owing to haemoglobin content) [29], magnetohydrodynamic (MHD) microfluidic platforms for cell switching [30], magneto-robotic endoscopy [31], electrocardiogram interaction with MHD [32], cardiac cycle synchronization of magnetic resonance imaging (MRI). Recent studies in computational simulations of magnetohydrodynamic medical flows have also examined a wide spectrum of applications including magneto-micro-robotic propulsion for embryological treatment [34], biomagnetic therapy [35], gastric endoscopy [36], bio-inspired nanofluid smart micro-pumps [37] and radiation tissue electromagnetic treatments [38]. These studies have confirmed that magnetic effects offer significant benefits in biomedical systems and have the advantage of being non-intrusive and relatively easy to implement [39].

Nanofluids comprise base fluids doped with nanoparticles and were introduced by Choi [40]. They offer considerable enhancement in thermal performance without the agglomeration and clustering issues associated with larger scale (micron) particles. They have also been shown to operate efficiently when combined with gyrotactic micro-organisms [41]. A powerful Hall voltage is developed by applying a strong magnetic field which is perpendicular to the current. The Hall parameter is compelling for immense magnetic field. The Hall current generates a secondary (cross) flow effect and is beneficial in furnishing an extra mechanism for regulating transport characteristics. Rotating viscous MHD flows with Hall current effects have received some attention in recent years both in physiological systems and industrial energy generation. Bég *et al.* [42] used PSPICE electro thermal network simulation to compute the hydromagnetic Newtonian flow in a rotating channel containing a permeable medium under oblique magnetic field with Hall current effect. They noted the significant acceleration in secondary flow with greater Hall current effect and a damping in the primary flow with increasing Hartmann number (magnetic body force number). Khan et al. [45] used a homotopy analysis method (HAM) to compute the unsteady hydromagnetic viscoelastic coating flow from a stretching surface with Hall current effect. They observed that axial flow acceleration is generated with stronger Hall current effect whereas deceleration is produced with stronger magnetic field. Bég et al. [46] used an implicit finite difference method (FDM) and Galerkin finite element method (FEM) to simulate the time-dependent hydromagnetic micropolar heat, mass and momentum transfer in channel flow with Hall and ion-slip current effects. Rotating disk swirling hydromagnetic

flow with Hall currents has been examined by Gaber and Mohamed [47] with wall (disk) suction and radiative heat transfer. Aboul-Hassanand Attia [48] investigated the swirling magnetohydrodynamic flow from a spinning disk with axial magnetic field and Hall effects. Mustafa et al. [49] studied the thermo-magnetic ferrofluid stagnation flow from a stretching spinning disk. Further studies include Thomas and Davies [50] and Béget al. [51].

In the present study, motivated by new developments in intelligent electromagnetic swirl bioreactor designs, we consider the combined effect of nanofluids and gyrotactic bioconvection in MHD Von Karman flow from a rotating radially stretching disk to a porous medium with Hall current effects. Anisotropic momentum slip, thermal slip, nanoparticle slip and micro-organism slip as well as Stefan blowing at the disk surface are also considered. Darcy's law is employed to model the porous medium drag force effect. Bacterial micro-organisms attach to the disk surface and begin to form cellulose as a gel that increases in thickness. Solid disks are inferior to disks that are perforated to allow improved film growth and therefore the presence of Stefan blowing is justified. The present study extends the earlier analysis of Bég et al. [52] to include magnetic field and Hall current effects. MATLAB bvp4c technique is achieved to find the numerical solutions [53]. The significance of Hall parameter, Darcy number, mass, circumferential and thermal slip, magnetic parameter, and Stefan suction/blowing on the velocity, temperature, nanoparticle concentration and micro-organism density number distributions is depicted graphically. Adomain decomposition method [54] is mobilized for the verification of the MATLAB solutions. The impact of selected parameters on skin friction, Nusselt number, Sherwood number and gradient of motile micro-organism density number are also tabulated.

2.MAGNETO-NANO-BIOCONVECTION SWIRLING FLOW MODEL

The physical regime to be studied is illuminated in Figure 1. Incompressible Von Karman swirling nanofluid flow of an magnetic fluid incorporating gyrotactic micro-organisms adjacent to a saturated homogenous, isotropic porous medium, is considered under an axial magnetic field, B_0. The disk radius is spanned with velocity in the radial direction. The disk spins at constant angular velocity Ω about the vertical axis, at $\bar{z}$. Anisotropic momentum slip, isotropic thermal jump (slip), isotropic nanoparticle slip, isotropic micro-organism slip and Stefan blowing effects are present. The strong magnetic field is applied perpendicular to the current which causes for the high voltage (Hall voltage) difference across the nanofluid. This Hall current yields the cross flow owing to the generation of radial forces. The magnetic nanoparticles added to the base fluid (water) are assumed dilute and do not alter the swimming direction or velocity of the micro-organisms. The resulting nanofluid has electrically conducting properties. However, magnetic Reynolds number is sufficiently small such that the magnetic field is not distorted, and magnetic induction effects are negated. The porous medium is non-deformable (rigid) and in thermal equilibrium with the swirling magnetic

nanofluid flow. A cylindrical co-ordinate system $(\bar{r}, \theta, \bar{z})$ is adopted with $(\bar{u}, \bar{v}, \bar{w})$ denoting the radial, tangential (azimuthal) and axial velocity components.

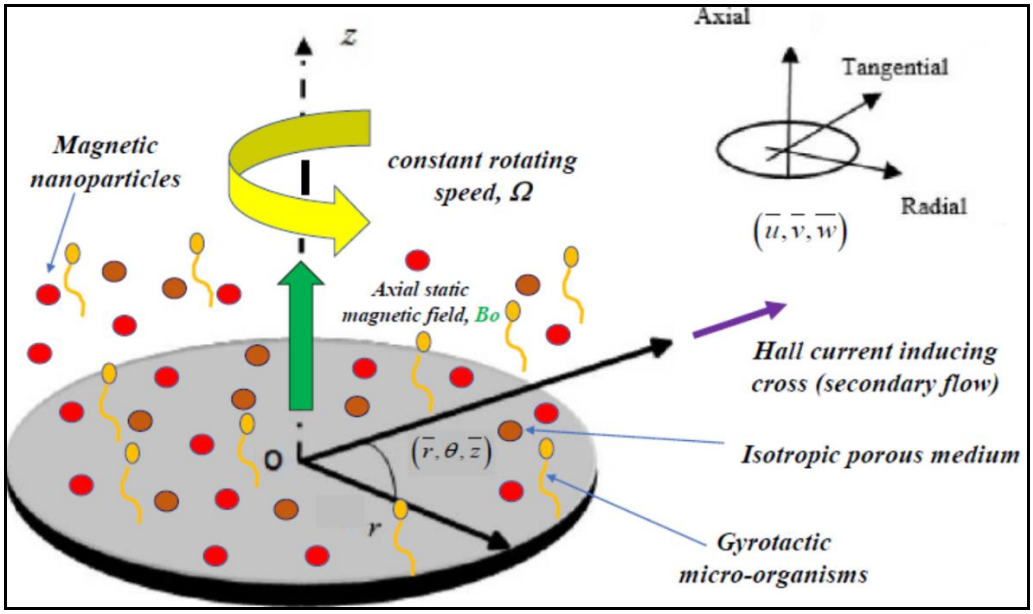

Fig. 1 Hall current magnetohydrodynamic nanofluid rotating bioreactor flow configuration

The rotating disk acts as a fluid pump and initially the nanofluid is at rest everywhere. Once rotation is initiated, the outward radial motion of the fluid close to the disk is compensated by an inward axial motion of the fluid towards the disk to conserve mass. Buongiorno's nanoscale model is employed and the Kuznetsov formulation employed for gyrotactic bioconvection [52]. The appropriate electromagnetic equations are as follows [55]:

Ohm's Law for moving conductor with Hall currents:

$$J + \frac{\omega_e \tau_e}{B}\left(J \times B\right) = \sigma\left(E + V \times B\right) \tag{1}$$

Maxwell Electromagnetic Equations:

$$\vec{\nabla}.B = \mu_e J \tag{2}$$

$$\vec{\nabla}.E = -\frac{\partial B}{\partial t} \tag{3}$$

$$\vec{\nabla}.J \neq 0 \tag{4}$$

$$\vec{\nabla}.B = 0 \tag{5}$$

Here $J = \left(J_r, J_\theta, J_z\right)$ is the electrical current density vector, B is the magnetic field vector $\left(B_r, B_\theta, B_z\right)$, E is the electrical field vector, σ, ω_e, τ_e are electrical conductivity, electron frequency, and electron collision time respectively. Furthermore, μ_e is the magnetic permeability of

the nanofluid. The electric field vanishes as there is no applied voltage $(E = 0)$. In the light of above used assumptions for a weakly ionized magnetic nanofluid, $J_\theta = 0$ everywhere in the flow, so comparing the *r*, *z* components, it follows that the current density has components J_r, J_z as follows, where B_z is taken as B_0:

$$J_x = \frac{\sigma\, B_0^2}{\left(1+h^2\right)\rho}\left(\bar{u} - h\bar{v}\right) \tag{6}$$

$$J_z = \frac{\sigma\, B_0^2}{\left(1+h^2\right)\rho}\left(h\bar{u} + \bar{v}\right) \tag{7}$$

where $h = \omega_e\, \tau_e$ is the Hall parameter. When the above Eqns. (6) and (7) are combined with the earlier non-magnetic model of Bég *et al*. [52], the resulting boundary layer equations for Von Karman swirling magnetohydrodynamic nanofluid bioconvection from the rotating disk assume the form:

Mass balance:

$$\frac{1}{\bar{r}}\frac{\partial}{\partial \bar{r}}\left(\bar{r}\,\bar{u}\right) + \frac{\partial \bar{w}}{\partial \bar{z}} = 0 \tag{8}$$

Momentum:

$$\bar{u}\frac{\partial \bar{u}}{\partial \bar{r}} + \bar{w}\frac{\partial \bar{u}}{\partial \bar{z}} - \frac{\bar{v}^2}{\bar{r}^2} = \upsilon\left(\frac{\partial^2 \bar{u}}{\partial \bar{r}^2} + \frac{1}{\bar{r}^2}\frac{\partial \bar{u}}{\partial \bar{r}} + \frac{\partial^2 \bar{u}}{\partial \bar{z}^2} - \frac{\bar{u}}{\bar{r}^2}\right) - \frac{\upsilon}{K\left(\frac{\bar{r}}{R}\right)}\bar{u} - \frac{\sigma\, B_0^2}{\left(1+h^2\right)\rho}\left(\bar{u} - h\bar{v}\right) \tag{9}$$

$$\bar{u}\frac{\partial \bar{v}}{\partial \bar{r}} + \bar{w}\frac{\partial \bar{v}}{\partial \bar{z}} + \frac{\bar{u}\,\bar{v}}{\bar{r}^2} = \upsilon\left(\frac{\partial^2 \bar{v}}{\partial \bar{r}^2} + \frac{1}{\bar{r}}\frac{\partial \bar{v}}{\partial \bar{r}} + \frac{\partial^2 \bar{v}}{\partial \bar{z}^2} - \frac{\bar{v}}{\bar{r}^2}\right) - \frac{\upsilon}{K\left(\frac{\bar{r}}{R}\right)}\bar{v} - \frac{\sigma\, B_0^2}{\left(1+h^2\right)\rho}\left(\bar{v} + h\bar{u}\right) \tag{10}$$

$$\bar{u}\frac{\partial \bar{w}}{\partial \bar{r}} + \bar{w}\frac{\partial \bar{w}}{\partial \bar{z}} = \upsilon\left(\frac{\partial^2 \bar{w}}{\partial \bar{r}^2} + \frac{1}{\bar{r}}\frac{\partial \bar{w}}{\partial \bar{r}} + \frac{\partial^2 \bar{w}}{\partial \bar{z}^2}\right) \tag{11}$$

Energy

$$\bar{u}\frac{\partial \bar{T}}{\partial \bar{r}} + \bar{w}\frac{\partial \bar{T}}{\partial \bar{z}} = \alpha\left(\frac{\partial^2 \bar{T}}{\partial \bar{r}^2} + \frac{1}{\bar{r}}\frac{\partial \bar{T}}{\partial \bar{r}} + \frac{\partial^2 \bar{T}}{\partial \bar{z}^2}\right) + \tau\, D_B\left(\frac{\partial \bar{C}}{\partial \bar{r}}\frac{\partial \bar{T}}{\partial \bar{r}} + \frac{\partial \bar{C}}{\partial \bar{z}}\frac{\partial \bar{T}}{\partial \bar{z}}\right) + \frac{\tau\, D_T}{T_\infty}\left(\left(\frac{\partial \bar{T}}{\partial \bar{r}}\right)^2 + \left(\frac{\partial \bar{T}}{\partial \bar{z}}\right)^2\right) \tag{12}$$

Nanoparticle volume fraction

$$\bar{u}\frac{\partial \bar{C}}{\partial \bar{r}} + \bar{w}\frac{\partial \bar{C}}{\partial \bar{z}} = D_B\left(\frac{\partial^2 \bar{C}}{\partial \bar{r}^2} + \frac{1}{\bar{r}}\frac{\partial \bar{C}}{\partial \bar{r}} + \frac{\partial^2 \bar{C}}{\partial \bar{z}^2}\right) + \frac{D_T}{T_\infty}\left(\frac{\partial^2 \bar{T}}{\partial \bar{r}^2} + \frac{1}{\bar{r}}\frac{\partial \bar{T}}{\partial \bar{r}} + \frac{\partial^2 \bar{T}}{\partial \bar{z}^2}\right) \tag{13}$$

Density number of motile organisms

$$\bar{u}\frac{\partial \bar{n}}{\partial \bar{r}} + \bar{w}\frac{\partial \bar{n}}{\partial \bar{z}} + \frac{\partial}{\partial \bar{z}}\left(\bar{n}\,\tilde{v}\right) = D_n\left(\frac{\partial^2 \bar{n}}{\partial \bar{r}^2} + \frac{1}{\bar{r}}\frac{\partial \bar{n}}{\partial \bar{r}} + \frac{\partial^2 \bar{n}}{\partial \bar{z}^2}\right) \tag{14}$$

The appropriate boundary conditions are [52]:

At $\bar{z} = 0$: (disk surface),

$$\bar{u} = N_1 \left(\frac{\bar{r}}{R}\right) \nu \frac{\partial \bar{u}}{\partial \bar{z}}, \qquad \bar{v} = N_2 \left(\frac{\bar{r}}{R}\right) \nu \frac{\partial \bar{v}}{\partial \bar{z}} + \left(\frac{\bar{r}}{R}\right)^{1-2m} \Omega R, \quad \bar{w} = -\frac{D_B}{1 - C_w} \frac{\partial \bar{C}}{\partial \bar{z}},$$
$$\bar{T} = T_w + D_1 \left(\frac{\bar{r}}{R}\right) \frac{\partial \bar{T}}{\partial \bar{z}}, \quad \bar{C} = C_w + E_1 \left(\frac{\bar{r}}{R}\right) \frac{\partial \bar{C}}{\partial \bar{z}}, \qquad \bar{n} = n_w + F_1 \left(\frac{\bar{r}}{R}\right) \frac{\partial \bar{n}}{\partial \bar{z}}. \tag{15}$$

As $\bar{z} \to +\infty$ (free stream),

$$\bar{u} \to 0, \quad \bar{v} \to 0, \quad \bar{T} \to T_\infty, \quad \bar{C} \to C_\infty, \quad \bar{n} \to n_\infty \tag{16}$$

where the meanings of notations used in Eqns. (8)-(14) are temperature (T), number of motile organisms (n), nanoparticle concentration (C), kinematic viscosity ν, density (ρ), constant permeability (K_0), variable permeability $\left(K = K_0\, r^{2m}\right)$, heat capacity of the fluid $(\rho c)_f$, heat capacity of the nanoparticles $(\rho\, c)_p$, thermal diffusivity (α), reference scale length (R), thermophoretic diffusion coefficient (D_T), surface temperature (T_w), ambient temperature (T_∞), microorganism diffusion coefficient (D_n), Brownian diffusion coefficient effective nanoparticles heat capacity (D_B), ambient mass concentration (C_∞), surface mass concentration (C_w), mass slip factor $\left(E_1 = (E_1)_0\, r^m\right)$, microorganism slip $\left(F_1 = (F_1)_0\, r^m\right)$, velocity slip along $\bar{u}$ $\left(N_1 = (N_1)_0\, r^m\right)$, velocity slip along $\bar{v}$ $\left(N_2 = (N_2)_0\, r^m\right)$, thermal slip factor $\left(D_1 = (D_1)_0\, r^m\right)$, chemotaxis constant $\left(\tilde{b}\right)$, maximum cell swimming speed (W_c), average directional swimming velocity of microorganisms $\left(\tilde{v} = \frac{\tilde{b}\, W_c}{\Delta C} \frac{\partial \bar{C}}{\partial \bar{z}}\right)$, wall motile microorganism density number (n_w). τ and m are dimensionless quantities representing the ratio of effective mangentic nanoparticle heat capacity to the fluid heat capacity and power law exponent respectively.

The nonlinear partial differential boundary value problem defined by Eqns. (11)-(16) are formidable to solve even with modern numerical methods. It is judicious to render the system non-dimensional and hence the following relations are implemented.

$$r = \frac{\bar{r}}{R}, \quad z = \frac{\bar{z}}{R}\sqrt{\mathrm{Re}}, \quad u = \frac{\bar{u}}{\Omega R}, \quad v = \frac{\bar{v}}{\Omega R}, \quad w = \frac{\bar{w}}{\Omega R}\sqrt{\mathrm{Re}},$$
$$\psi = \frac{\bar{n}}{n_w}, \quad \theta = \frac{\bar{T} - T_\infty}{T_w - T_\infty}, \quad \phi = \frac{\bar{C} - C_\infty}{C_w - C_\infty} \tag{17}$$

Implementing Eqn. (17) the non-dimensional boundary layer equations emerge as:

$$\frac{\partial u}{\partial r}+\frac{u}{r}+\frac{\partial w}{\partial z}=0 \tag{18}$$

$$u\,\frac{\partial u}{\partial r}+w\,\frac{\partial u}{\partial z}-\frac{v^2}{r}=\frac{1}{\mathrm{Re}}\left(\frac{\partial^2 u}{\partial r^2}+\frac{1}{r}\frac{\partial u}{\partial r}-\frac{u}{r^2}\right)+\frac{\partial^2 u}{\partial z^2}-\frac{\mu}{\rho\Omega K_0 r^{2m+1}}u-\frac{M\left(u-hv\right)}{r^{2m}} \tag{19}$$

$$u\,\frac{\partial v}{\partial r}+w\,\frac{\partial v}{\partial z}+\frac{uv}{r}=\frac{1}{\mathrm{Re}}\left(\frac{\partial^2 v}{\partial r^2}+\frac{1}{r}\frac{\partial v}{\partial r}-\frac{v}{r^2}\right)+\frac{\partial^2 v}{\partial z^2}-\frac{M}{\rho\Omega K_0 r^{2m+1}}v-\frac{M\left(v+hu\right)}{r^{2m}} \tag{20}$$

$$u\,\frac{\partial w}{\partial r}+w\,\frac{\partial w}{\partial z}=\frac{1}{\mathrm{Re}}\left(\frac{\partial^2 w}{\partial r^2}+\frac{1}{r}\frac{\partial w}{\partial r}\right)+\frac{\partial^2 w}{\partial z^2} \tag{21}$$

$$\begin{aligned} u\,\frac{\partial \theta}{\partial r}+w\,\frac{\partial \theta}{\partial z}=&\frac{1}{\mathrm{Pr}\ \mathrm{Re}}\left(\frac{\partial^2\theta}{\partial r^2}+\frac{1}{r}\frac{\partial\theta}{\partial r}+\frac{Nb}{\mathrm{Pr}}\frac{\partial\theta}{\partial r}\frac{\partial\phi}{\partial r}+\frac{Nt}{\mathrm{Pr}}\left(\frac{\partial\theta}{\partial r}\right)^2\right)+\\ &\frac{1}{\mathrm{Pr}}\left(\frac{\partial^2\theta}{\partial z^2}+Nb\left(\frac{\partial\theta}{\partial z}\frac{\partial\phi}{\partial z}\right)+Nt\left(\frac{\partial\theta}{\partial r}\right)^2\right) \end{aligned} \tag{22}$$

$$\begin{aligned} u\,\frac{\partial \phi}{\partial r}+w\,\frac{\partial \phi}{\partial z}=&\frac{1}{Le\ \mathrm{Pr}\ \mathrm{Re}}\left(\frac{\partial^2\phi}{\partial r^2}+\frac{1}{r}\frac{\partial\phi}{\partial r}+\frac{Nt}{Nb}\left(\frac{\partial^2\theta}{\partial r^2}+\frac{1}{r}\frac{\partial\theta}{\partial r}\right)\right)+\\ &\frac{1}{\mathrm{Pr}\ Le}\left(\frac{\partial^2\phi}{\partial z^2}+\frac{Nb}{Nt}\left(\frac{\partial^2\phi}{\partial z^2}\right)\right) \end{aligned} \tag{23}$$

$$u\,\frac{\partial \psi}{\partial r}+w\,\frac{\partial \psi}{\partial z}=\frac{1}{Sb}\frac{\partial^2\psi}{\partial r^2}-\frac{Pe}{Sb}\left(\frac{\partial\psi}{\partial z}\frac{\partial\phi}{\partial z}+\psi\frac{\partial^2\phi}{\partial z^2}\right) \tag{24}$$

The dimensionless boundary conditions at the disk surface and in the free stream (edge of the boundary layer) take the form:

$$\left.\begin{aligned} &u=N_1(r)\,\frac{\nu\sqrt{\mathrm{Re}}}{R}\frac{\partial u}{\partial z};\quad v=N_2(r)\,\frac{\nu\sqrt{\mathrm{Re}}}{R}\frac{\partial v}{\partial z}+r^{1-2m};\quad w=-\frac{s}{\mathrm{Pr}\ Le}\frac{\partial\phi}{\partial z};\\ &\theta=D_1(r)\,\frac{\sqrt{\mathrm{Re}}}{R}\frac{\partial\theta}{\partial z}+1;\quad \phi=E_1(r)\,\frac{\sqrt{\mathrm{Re}}}{R}\frac{\partial\phi}{\partial z}+1;\quad \psi=F_1(r)\,\frac{\sqrt{\mathrm{Re}}}{R}\frac{\partial\psi}{\partial z}+1 \end{aligned}\right\}\ \text{at}\ \ z=0 \tag{25}$$

$$\left.u\to 0;\quad v\to 0;\quad \theta\to 0;\quad \phi\to 0;\quad \psi\to 0\right\}\quad \text{as}\ \ z\to\infty \tag{26}$$

The dimensionless boundary value problem defined by Eqns. (18)-(26) may further be simplified by deploying the relations as follows:

$$\begin{aligned} &\eta=z\,r^{-m},\quad u=r^{1-2m}\,f'(\eta),\quad v=r^{1-2m}\,g(\eta),\quad w=-r^{-m}\left((2-m)\,f(\eta)-m\eta\,f'(\eta)\right),\\ &\theta=\theta(\eta),\ \phi=\phi(\eta),\quad \psi=\psi(\eta) \end{aligned} \tag{27}$$

Substituting Eqn. (27) into Eqns. (18)-(24), wherein the continuity equation is automatically satisfied. The generated nonlinear ordinary differential equations are:

$$f'''+(2-m)\,f\,f''-(1-2m)(f')^2+g^2-\frac{1}{Da}f'-M\left(f'-hg\right)=0 \tag{28}$$

$$g'' + (2-m)\, f\, g' - (2-2m)\, f'\, g - \frac{1}{Da} g - M\,(g + h\, f') = 0 \tag{29}$$

$$\theta'' + \mathrm{Pr}\,(2-m)\, f\, \theta' + Nb\, \theta'\, \phi' + Nt\, (\theta')^2 = 0 \tag{30}$$

$$\phi'' + \mathrm{Pr}\; Le\; (2-m)\, f\, \phi' + \frac{Nt}{Nb}\, \theta'' = 0 \tag{31}$$

$$\psi'' + Sb\; (2-m)\, f\, \psi' - Pe\, (\psi'\, \phi' + \psi\, \phi'') = 0 \tag{32}$$

In Eqs. (28) to (32) f corresponds to $f(\eta)$ i.e. dimensionless stream function.
The conditions on the boundary as given in Eqs. (25) and (26) emerge as:

$$\left.\begin{array}{l} f'(0) = \delta_u\; f''(0); \quad g(0) = 1 + \delta_v\; g'(0); \quad f(0) = \dfrac{s}{\mathrm{Pr}\; Le\,(2-m)}\, \phi'(0); \\ \theta(0) = 1 + \delta_T\; \theta'(0); \;\; \phi(0) = 1 + \delta_c\; \phi'(0); \quad \psi(0) = 1 + \delta_n\; \chi'(0) \end{array}\right\} \text{ at } \eta = 0 \tag{33}$$

$$\left.\begin{array}{l} f'(+\infty) \to 0; \; g(+\infty) \to 0; \; \theta(+\infty) \to 0; \; \phi(+\infty) \to 0; \; \chi(+\infty) \to 0 \end{array}\right\} \text{ as } \eta \to \infty \tag{34}$$

In Eqns. (28)-(32), the non-dimensional parameters are: axial stream function (f), circumferential stream function (g), temperature (θ), nanoparticle concentration (ϕ), motile microorganism density number (ψ), rotational Reynolds number $\left(\mathrm{Re} = \dfrac{\Omega\, R^2}{\nu}\right)$, the magnetic interaction parameter $\left(M = \dfrac{\sigma\, B_0^2}{\Omega\, \rho}\right)$, Darcy number $\left(Da = \dfrac{r\, \Omega K_0}{\nu}\right)$, Prandtl number $\left(\mathrm{Pr} = \dfrac{\nu}{\alpha}\right)$, bioconvection Péclet number $\left(Pe = \dfrac{\tilde{b}\, W_c}{D_B}\right)$, Lewis number $\left(Le = \dfrac{\alpha}{D_B}\right)$, Brownian motion $\left(Nb = \dfrac{\tau D_B\, \Delta C}{\alpha}\right)$, thermophoresis $\left(Nt = \dfrac{\tau\; D_T\, \Delta T}{\alpha T_\infty}\right)$, bioconvection Schmidt number $\left(Sb = \dfrac{\nu}{D_B}\right)$, radial momentum slip $\left(\delta_u = \dfrac{(N_1)_0\; \nu\; \sqrt{\mathrm{Re}}}{R}\right)$, circumferential (tangential) momentum slip $\left(\delta_v = \dfrac{(N_2)_0\; \nu\; \sqrt{\mathrm{Re}}}{R}\right)$, thermal slip $\left(\delta_T = \dfrac{(D_1)_0\; \nu\; \sqrt{\mathrm{Re}}}{R}\right)$, mass slip $\left(\delta_c = \dfrac{(E_1)_0\; \nu\; \sqrt{\mathrm{Re}}}{R}\right)$, microorganism slip $\left(\delta_n = \dfrac{(F_1)_0\; \nu\; \sqrt{\mathrm{Re}}}{R}\right)$, Stefan blowing parameter $\left(s = \dfrac{\Delta C}{1 - C_w}\right)$.

The positive values of s implies that the mass flux moves from the disk to the free stream and the opposite trend is attained for negative values of s (Bég *et al.* [52] and Fang [56]). Key engineering design quantities are the *gradients of the transport functions* at the disk surface (wall) and these are defined mathematically as, radial local skin friction along $\bar{r}$ -direction $\left(C_{f\bar{r}} = \dfrac{\tau_{\bar{r}}}{\rho_f\; \bar{u}^2}\right)$, tangential

local skin friction along θ-direction $\left(C_{f\theta} = \frac{\tau_\theta}{\rho_f \ \bar{v}^2} \right)$, Nusselt number $\left(Nu_{\bar{r}} = \frac{\bar{r} \ q_w}{k_f \ (T_w - T_\infty)} \right)$, Sherwood number $\left(Sh_{\bar{r}} = \frac{\bar{r} \ q_m}{D_B \ (C_w - C_\infty)} \right)$ and wall motile microorganism $\left(Nn_{\bar{r}} = \frac{\bar{r} \ q_n}{D_n \ n_w} \right)$ where

$\tau_{\bar{r}} = \mu \left(\frac{\partial \bar{u}}{\partial \bar{z}} + \frac{\partial \bar{w}}{\partial \bar{r}} \right)_{\bar{z}=0}$, $\tau_\theta = \mu \left(\frac{\partial \bar{v}}{\partial \bar{z}} + \frac{\partial \bar{w}}{\partial \bar{r}} \right)_{\bar{z}=0}$, $q_w = -k \left(\frac{\partial T}{\partial \bar{z}} \right)_{\bar{z}=0}$, $q_m = -D_B \left(\frac{\partial C}{\partial \bar{z}} \right)_{\bar{z}=0}$,

$q_n = -D_n \left(\frac{\partial n}{\partial \bar{z}} \right)_{\bar{z}=0}$.

Using Eqn. (18), the expressions become $\sqrt{\mathrm{Re}_{\bar{r}}} \ C_{f\bar{r}} = f''(0)$, $\sqrt{\mathrm{Re}_{\bar{r}}} \ C_{f\theta} = g'(0)$, $\frac{1}{\sqrt{\mathrm{Re}_{\bar{r}}}} Nu_{\bar{r}} = -\theta'(0)$, $\frac{1}{\sqrt{\mathrm{Re}_{\bar{r}}}} Sh_{\bar{r}} = -\phi'(0)$, $\frac{1}{\sqrt{\mathrm{Re}_{\bar{r}}}} Nn_{\bar{r}} = -\psi'(0)$ where $\mathrm{Re}_{\bar{r}} = \frac{\Omega \ R^2}{\nu \ r^{2(m-1)}}$ is the local rotational Reynolds number.

3. COMPUTATIONAL SOLUTION WITH MATLAB BVP4C AND VALIDATION

The dimensionless 11th order non-linear ordinary differential boundary value problem (BVP) defined by Eqns. (28)-(32) with boundary conditions (33, 34) may be solved with a variety of numerical methods. Here we adopt the MATLAB bvp4c routine [53]. The finite difference-based boundary value problem solver bvp4c tool in MATLAB is very efficient at solving nonlinear coupled higher order differential equations. The iterative process is carried out until the accuracy of 10^{-6} and this is obtained for the values of $\eta_\infty = 7$ and $\Delta\eta = 0.001$ (step size). The fourth-order formulae are given below:

$$k_1 = h \ f(x_n, \ y_n)$$

$$k_2 = h \ f\left(x_n + \frac{h}{2}, \ y_n + \frac{k_1}{2} \right)$$

$$k_3 = h \ f\left(x_n + \frac{h}{2}, \ y_n + \frac{k_2}{2} \right)$$

$$k_4 = h \ f(x_n + h, \ y_n + k_3)$$

$$y_{n+1} = y_n + \frac{k_1}{6} + \frac{k_2}{3} + \frac{k_3}{3} + \frac{k_4}{6} + O(h^5) \tag{35}$$

The above-described computing approach cannot be used without transforming the higher-order differential equations to differential equations of order one. The mathematical process is described as follows:

$$f = y_1, \quad f' = y_2, \quad f'' = y_3$$
$$g = y_4, \quad g' = y_5$$
$$\theta = y_6, \quad \theta' = y_7 \tag{36}$$
$$\phi = y_8, \quad \phi' = y_9$$
$$\psi = y_{10}, \quad \psi' = y_{11}$$

$$f''' = (1-2m)\, y_2^2 - (2-m)\, y_1\, y_3 - y_4^2 + \frac{1}{Da}\, y_2 + M\,(y_2 - h\, y_4) \tag{37}$$

$$g'' = -(2-m)\, y_1\, y_5 + (2-2m) y_2\, y_4 + \frac{1}{Da}\, y_4 + M\,(y_4\, h\, y_2) \tag{38}$$

$$\theta'' = -\,\mathrm{Pr}\,(2-m)\, y_1\, y_7 - Nb\, y_7\, y_9 - Nt\, y_7^2 \tag{39}$$

$$\phi'' = (m-2)\, Le\,\mathrm{Pr}\, y_1\, y_9 - \frac{Nt}{Nb}\left[(m-2)\,\mathrm{Pr}\, y_1\, y_7 - Nb\, y_7\, y_9 - Nt\, y_7^2\right] \tag{40}$$

$$\psi'' = Sb\,(m-2)\, y_1\, y_{11} + Pe\left[y_{11}\, y_9 + y_{10}\left[(m-2)\, Le\,\mathrm{Pr}\, y_1\, y_9 - \frac{Nt}{Nb}\left((m-2)\,\mathrm{Pr}\, y_1\, y_7 - Nb\, y_7\, y_9 - Nt\, y_7^2\right)\right]\right] \tag{41}$$

Corresponding boundary conditions become

$$\left.\begin{aligned} y_2(0) &= \delta_4\; y_3(0) \\ y_4(0) &= 1 + \delta_v\; y_5(0) \\ y_1(0) &= \frac{S}{Le\,\mathrm{Pr}\,(2-m)}\, y_9(0) \\ y_6(0) &= 1 + \delta_T\; y_7(0) \\ y_{10}(0) &= 1 + \delta_n\; y_{11}(0) \end{aligned}\right\} \; at\ \eta = 0 \tag{42}$$

$$\left.\begin{aligned} y_2(+\infty) \to 0;\; y_4(+\infty) \to 0;\; y_6(+\infty) \to 0;\; y_8(+\infty) \to 0;\; y_{10}(+\infty) \to 0 \end{aligned}\right\} \; as\ \eta \to \infty \tag{43}$$

Table 1: Validation of MATLAB solutions with Chebychev collocation solutions of Bég *et al.* [52] for $M = 0.0,\ h = 0.0, m = -0.5, Da = 10.0, Pr = 6.8, Nb = Nt = 0.1, Le = Pe = Sb = 1.0,$ $\delta_u = 0.0,\ \delta_v = \delta_\theta = \delta_c = \delta_n = 0.1$

	Bég *et al.* [52]					Present MATLAB bvp4c solutions				
	$f''(0)$	$-g'(0)$	$-\theta'(0)$	$-\phi'(0)$	$\chi'(0)$	$f''(0)$	$-g'(0)$	$-\theta'(0)$	$-\phi'(0)$	$\chi'(0)$
s										
−1	0.4151	0.6456	1.1192	0.6302	0.8583	0.3931	0.67876	1.0862	0.60573	0.82775
0	0.4204	0.6118	0.8196	0.596	0.7833	0.39874	0.64618	0.79628	0.57374	0.7541
1	0.4245	0.5835	0.5869	0.5558	0.7086	0.40292	0.61853	0.57085	0.535	0.68146

MATLAB bvp4c has been deployed extensively in many multi-physical fluid dynamics problems and further details are given in Yoo [53]. Validation with the earlier Chebychev collocation non-magnetic $(M = 0.0,\ h = 0.0)$ solutions of Bég *et al.* [52] has been conducted and are shown in Table 1. Generally good correlation is arrived asserting to the efficiency and reliability of the present MATLAB code.

4. FURTHER AFFIRMATION USING ADM (ADOMIAN DECOMPOSITION METHOD)

To further validate the magnetic nanofluid bioconvection model solutions obtained with MATLAB, a different approach is required which provides a much more rigorous verification than merely benchmarking with existing simpler cases from the literature. ADM (Adomian [54]) is implemented. ADM is very flexible and is used recently to solve stagnation coating flows [58], intelligent magnetic squeeze orthopedic lubrication problems [59], spin coating flows [60] and electromagnetic pumping [61]. Implementing ADM, we adopt the following notation:

$L_1 = \dfrac{d^3}{d\eta^3}(\ )$ and $L_2 = \dfrac{d^2}{d\eta^2}(\ )$ and their inverse operators are:

$$L_1^{-1}(\ ) = \int_0^\eta \int_0^\eta \int_0^\eta (\ )\, d\eta\, d\eta\, d\eta \quad \text{and} \quad L_2^{-1}(\ ) = \int_0^\eta \int_0^\eta (\ )\, d\eta\, d\eta \tag{36}$$

The unknown functions $f, g, \theta, \phi,$ and ψ are asserted in the Adomian polynomials as :

$$f(n) = \sum_{m=0}^{\infty} f_m\ ,\quad g(n) = \sum_{m=0}^{\infty} g_m\ ,\quad \theta(n) = \sum_{m=0}^{\infty} \theta_m\ ,\quad \phi(n) = \sum_{m=0}^{\infty} \phi_m\ ,\quad \psi(n) = \sum_{m=0}^{\infty} \psi_m \tag{37}$$

The exact solutions are developed as:

$$f(n) = Lim \sum_{m=0}^{\infty} f_m,\ \ g(n) = Lim \sum_{m=0}^{\infty} g_m,\ \ \theta(n) = Lim \sum_{m=0}^{\infty} \theta_m,\ \ \phi(n) = Lim \sum_{m=0}^{\infty} \phi_m,\ \ \psi(n) = Lim \sum_{m=0}^{\infty} \psi_m \tag{38}$$

Excellent correlation is achieved for all variables at all values of parameters between MATLAB bvp4c and ADM as noticed in Table 2. Confidence in the MATLAB code is therefore again strongly demonstrated.

Table 2: MATLAB versus ADM solutions for $f''(0), g'(0), \theta'(0), \phi'(0), \psi'(0)$ with $M = 0.5,\ h = 0.1,\ m = -0.5,\ Da = 10.0,\ \mathrm{Pr} = 6.0,\ Nt = Nb = 0.1,\ Sb = Pe = Le = 1,$ $\delta_u = 0.1,\ \delta_v = 0.1,\ \delta_T = 0.1,\ \delta_c = 0.1,\ \delta_n = 0.1$ (unless otherwise indicated).

	$f''(0)$ MATLAB	$f''(0)$ ADM	$-g'(0)$ MATLAB	$-g'(0)$ ADM	$-\theta'(0)$ MATLAB	$-\theta'(0)$ ADM	$-\phi'(0)$ MATLAB	$-\phi'(0)$ ADM	$-\psi'(0)$ MATLAB	$-\psi'(0)$ ADM
	$\delta_u = 0.5$									
S										
- 1	0.12179	0.11946	1.36630	1.36624	0.84714	0.84709	0.36994	0.36987	0.55895	0.55892

0	0.12389	0.12104	1.34430	1.34419	0.64209	0.64204	0.32987	0.32978	0.48639	0.48631
1	0.12554	0.12478	1.32700	1.32707	0.48817	0.48808	0.29583	0.29591	0.42811	0.42823
	$\delta_v = 0.5$									
S										
- 1	0.17291	0.17307	0.63527	0.63521	0.80125	0.80133	0.39810	0.39804	0.58312	0.58308
0	0.17791	0.17803	0.62135	0.62129	0.59620	0.59627	0.37411	0.37406	0.52507	0.52513
1	0.18213	0.18194	0.60939	0.60944	0.43698	0.43691	0.34751	0.34742	0.47115	0.47123
	$\delta_T = 0.5$									
S										
- 1	0.23032	0.23103	1.03970	1.03965	0.68793	0.68788	0.58142	0.58137	0.76218	0.76211
0	0.23561	0.23612	1.00270	1.00267	0.50701	0.50707	0.43852	0.43847	0.58364	0.58372
1	0.23032	0.23104	1.03970	1.03964	0.68793	0.68784	0.58142	0.58135	0.76218	0.76213
	$\delta_c = 0.5$									
S										
- 1	0.28054	0.28061	0.89723	0.89732	0.90254	0.90247	0.35070	0.35066	0.58377	0.58372
0	0.28419	0.28407	0.87530	0.87526	0.72782	0.72776	0.35382	0.35378	0.55475	0.55468
1	0.28764	0.28758	0.85376	0.85368	0.56639	0.56643	0.35265	0.35271	0.52293	0.52288
	$\delta_n = 0.5$									
S										
- 1	0.27893	0.27889	0.90669	0.90661	0.97436	0.97431	0.49961	0.49958	0.55636	0.55631
0	0.28419	0.28406	0.87530	0.87526	0.72334	0.72342	0.46755	0.46759	0.51066	0.51062
1	0.28642	0.28639	0.86146	0.86138	0.61870	0.61864	0.45128	0.45132	0.48880	0.48877
	$M = 0.5$									
S										
- 1	0.23767	0.23759	1.35300	1.35289	0.78610	0.78603	0.35962	0.35957	0.53928	0.53922
0	0.24003	0.24011	1.33110	1.33099	0.58794	0.58788	0.32319	0.32323	0.47120	0.47131
1	0.24187	0.24182	1.31360	1.31358	0.43988	0.43979	0.29050	0.29046	0.41490	0.41503
	$h = 1.5$									
S										
- 1	0.47001	0.47004	1.07310	1.07304	1.22000	1.22004	0.65454	0.65459	0.91629	0.91623
0	0.47661	0.47653	1.03260	1.03256	0.90532	0.90526	0.61029	0.61037	0.82057	0.82065
1	0.48168	0.48171	0.99839	0.99832	0.65985	0.65989	0.56624	0.56628	0.73462	0.73471

5. RESULTS AND DISCUSSION

MATLAB bvp4c computations are visualized in Figs 2- 11. Aqueous magnetic nanofluid is considered (Prandtl number is generally prescribed as Pr=6.0 or 6.8 which has a value below that of pure water due to the presence of magnetic nanoparticles which increase thermal conductivity). The following default data is utilized, following Bég *et al.* [52], Foster and Schwan [62] and Kuure-Kinsey *et al.* [63]. The fixation values are same as shown in the tables, except the variable parameter in the figures. This data corresponds to intermediate strength magnetic field and nanoscale effects, high permeability porous media and strong bioconvection with weak anisotropic momentum and

other slip effects at the disk surface. As noted earlier, in all plots, an infinity boundary condition of $\eta = 7$ is prescribed which achieves asymptotically smooth solutions for the condition, $\eta \to \infty$.

(a)

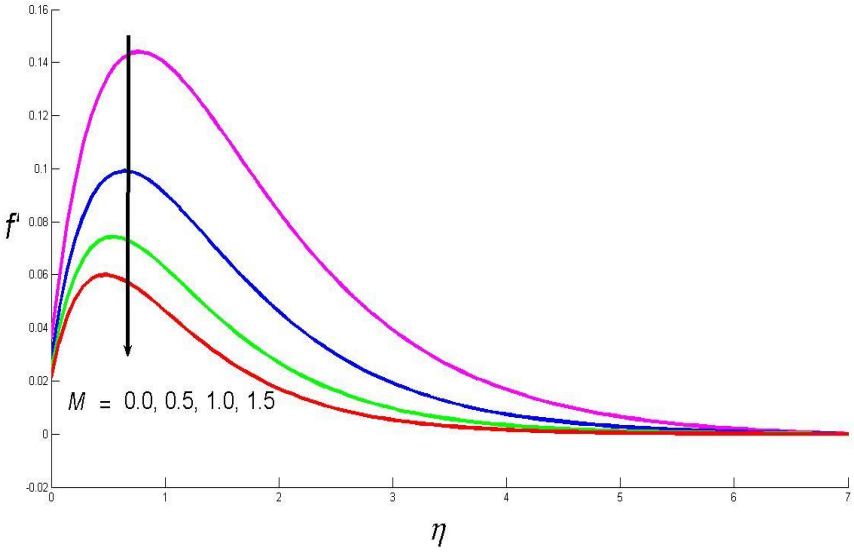

(b)

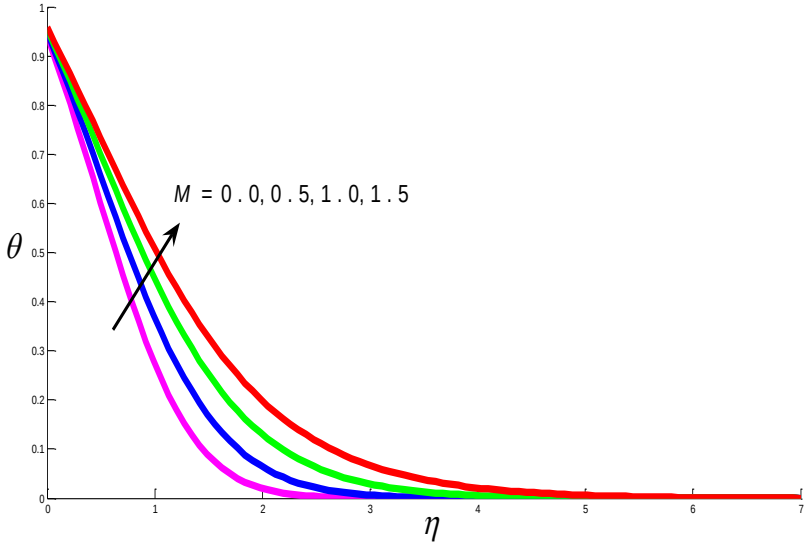

(c)

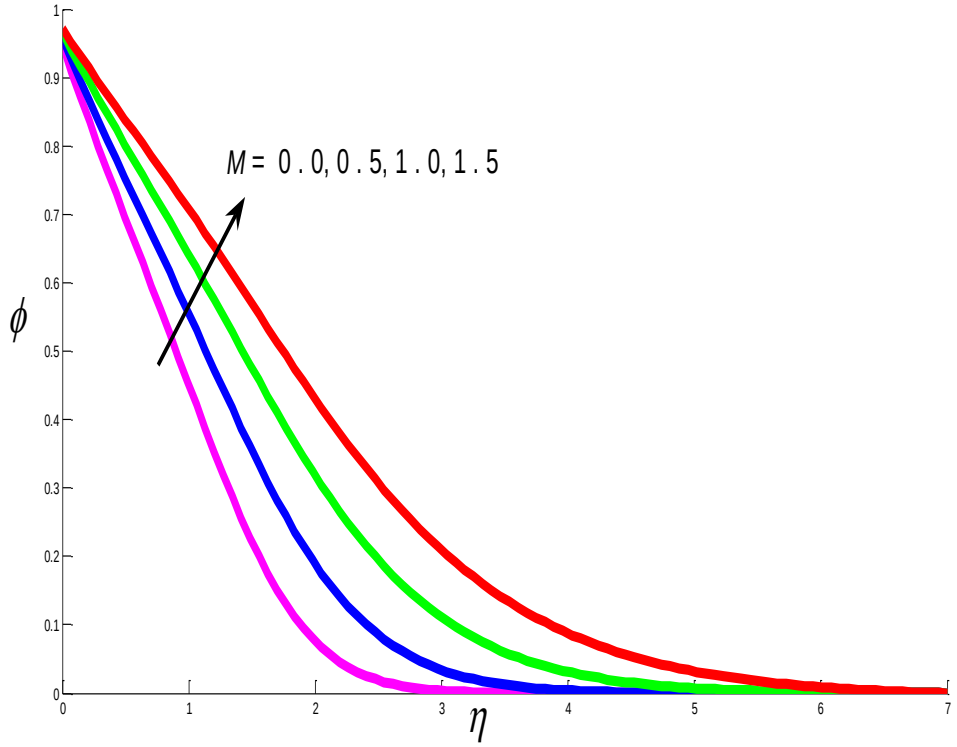

(d)

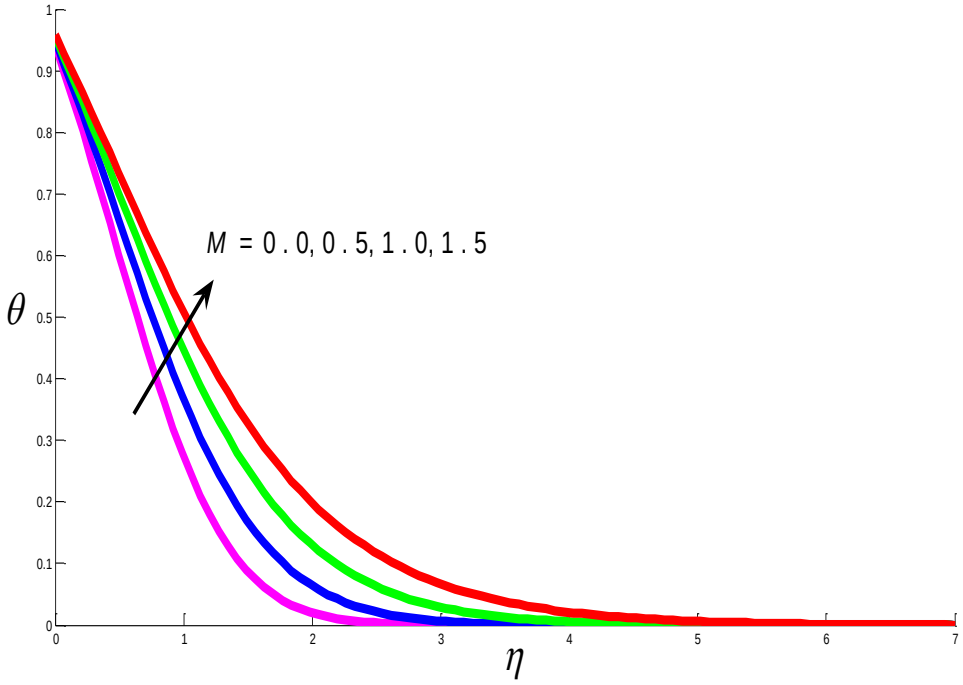

Figure 2. Profiles for different magnetic interaction number, M

(a)

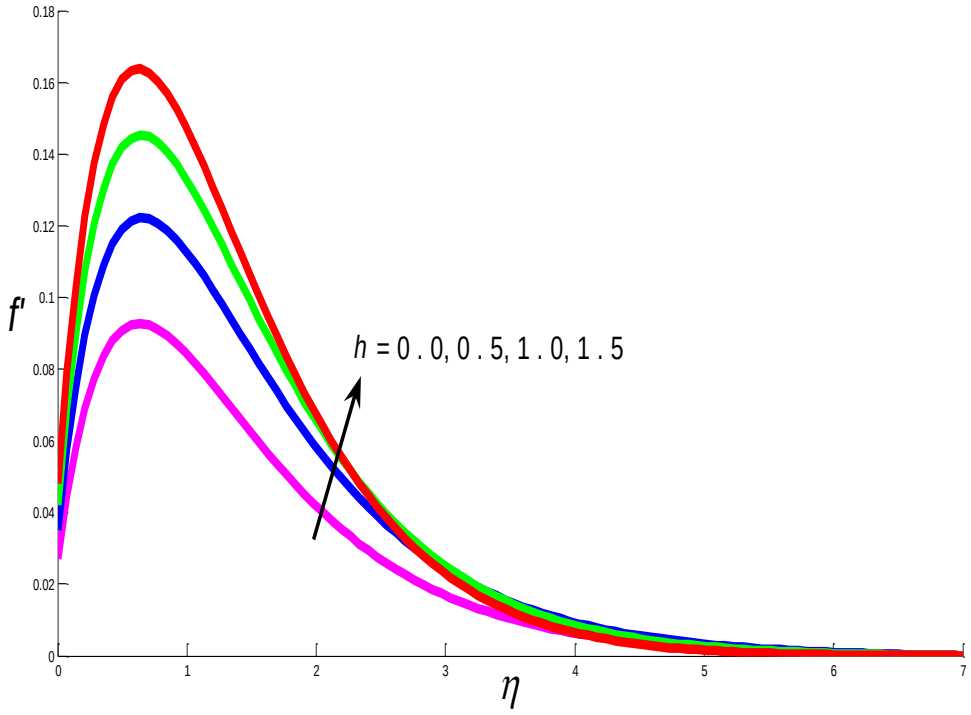

(b)

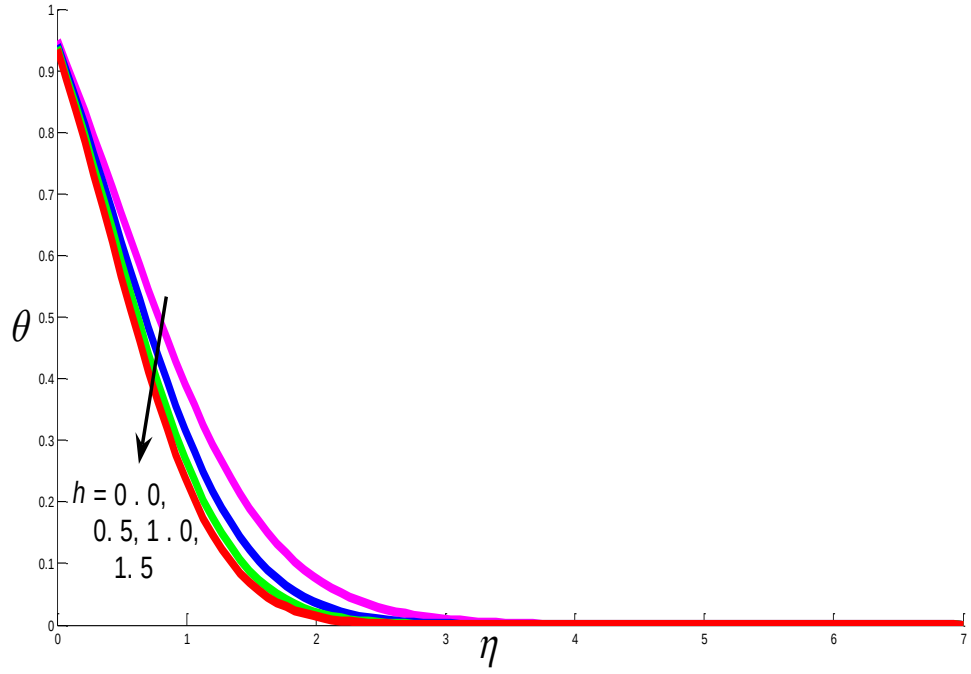

(c)

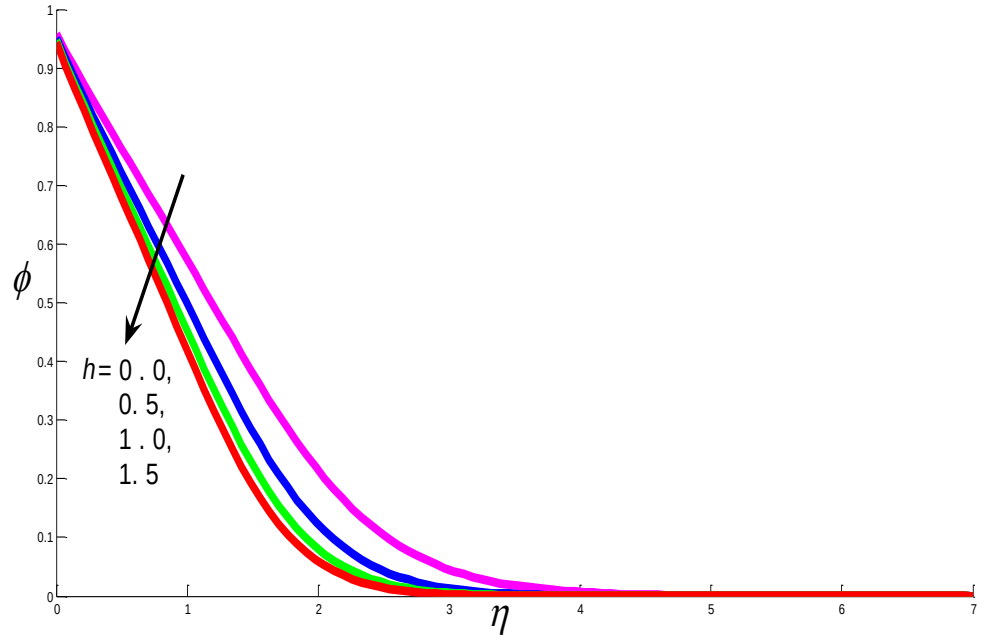

(d)

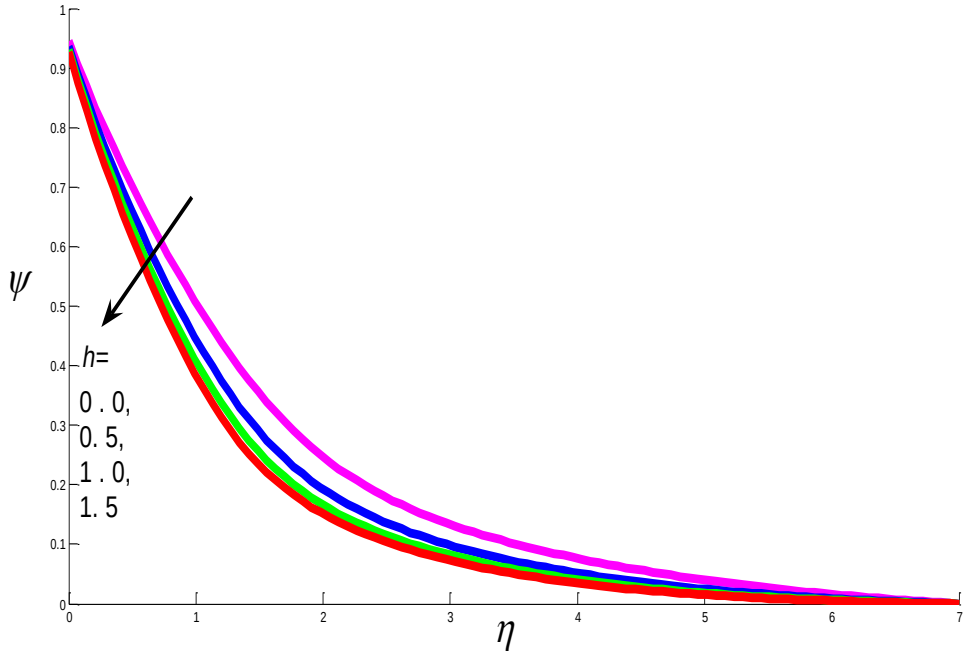

Figure 3: Profiles for different Hall current parameter h

(a)

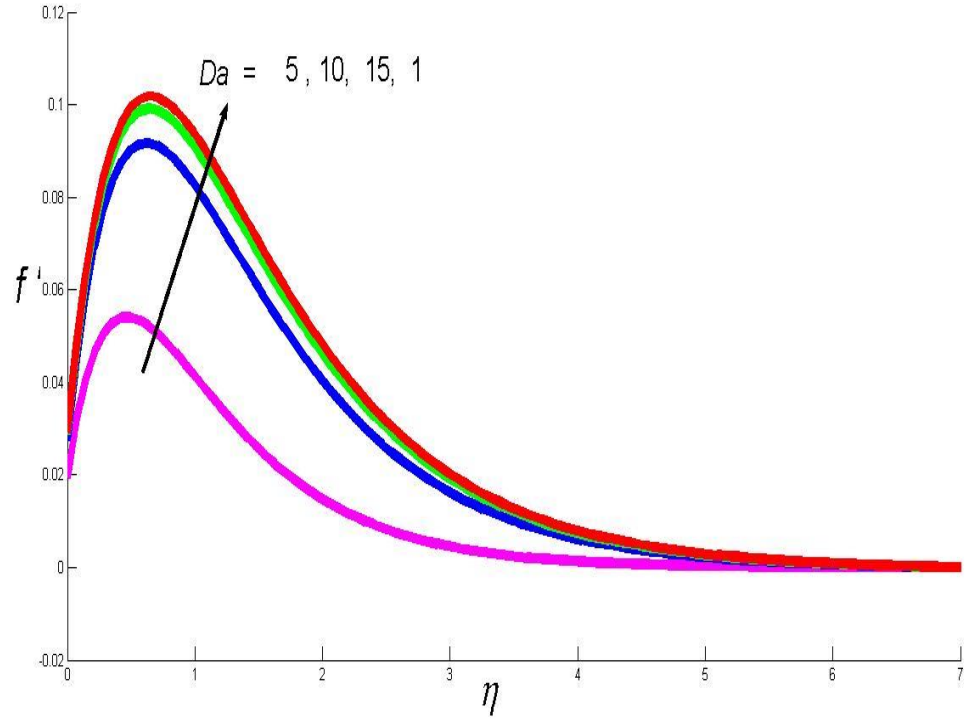

(b)

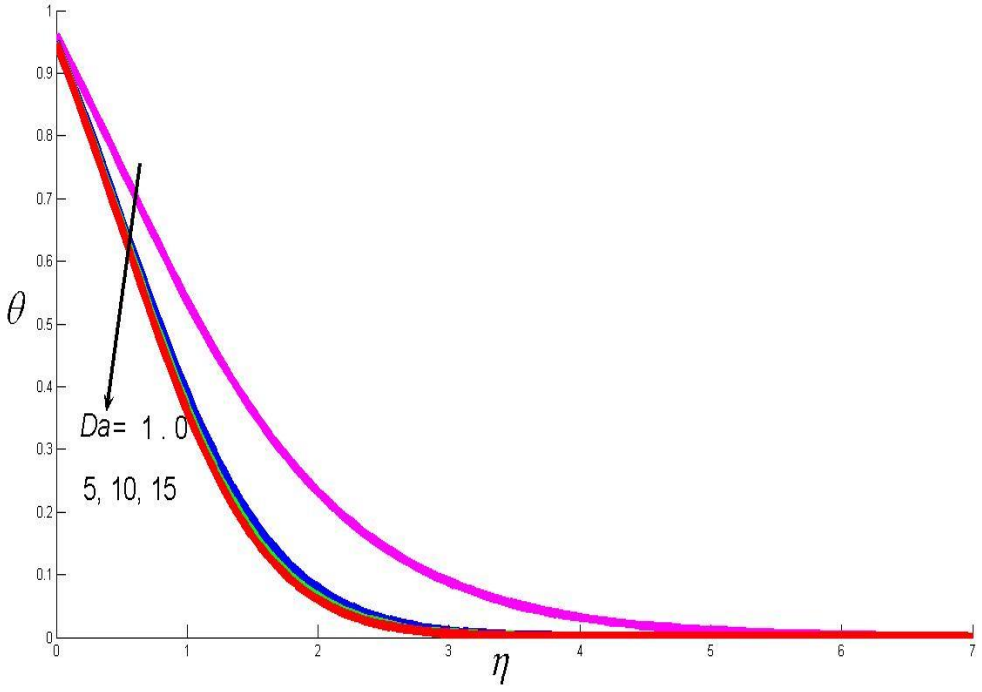

(c)

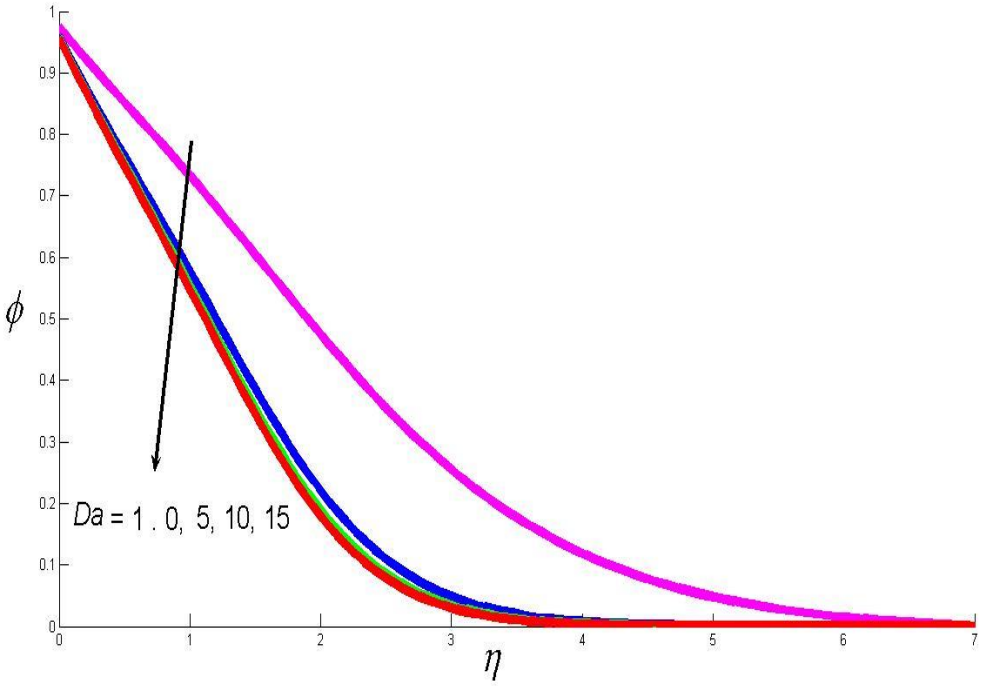

(d)

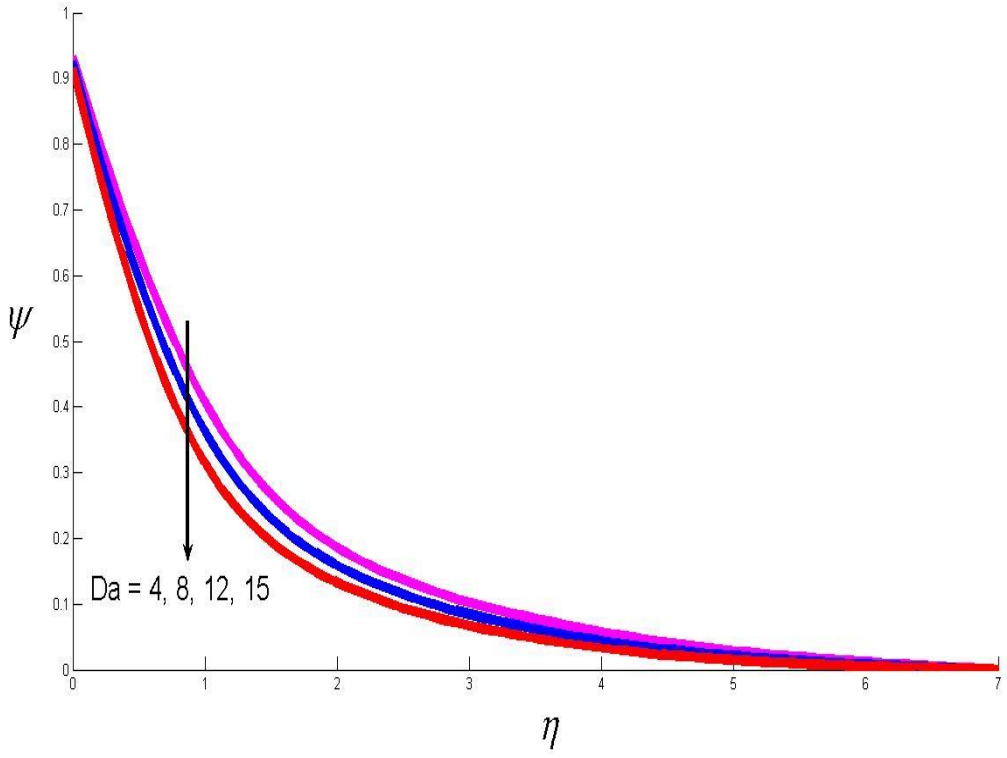

Figure 4 Profiles for different Darcy number *Da*

(a)

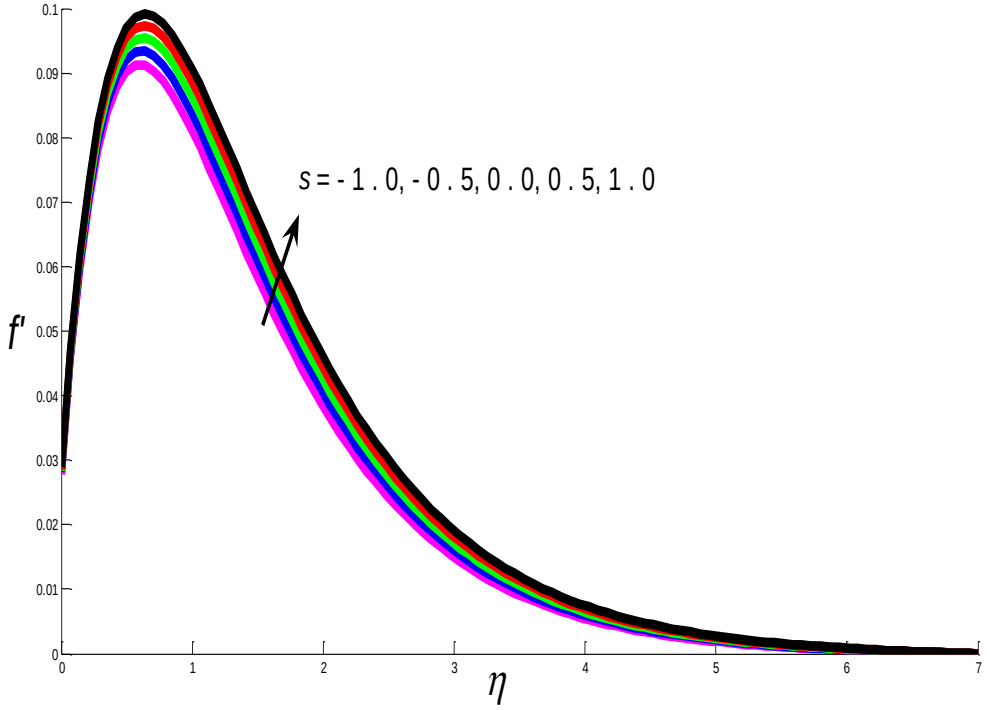

(b)

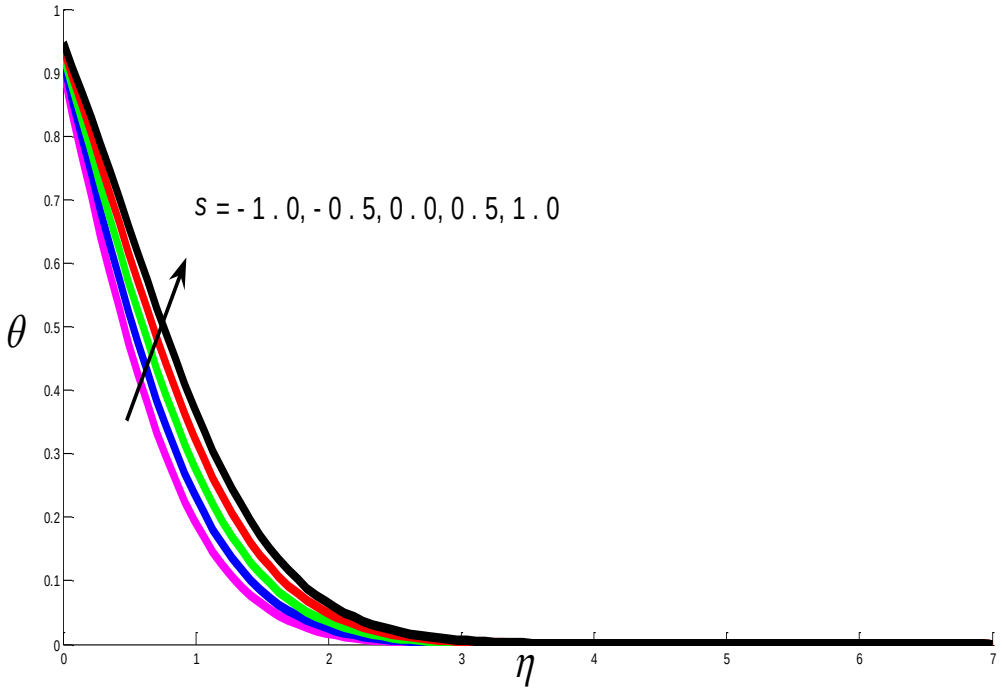

(c)

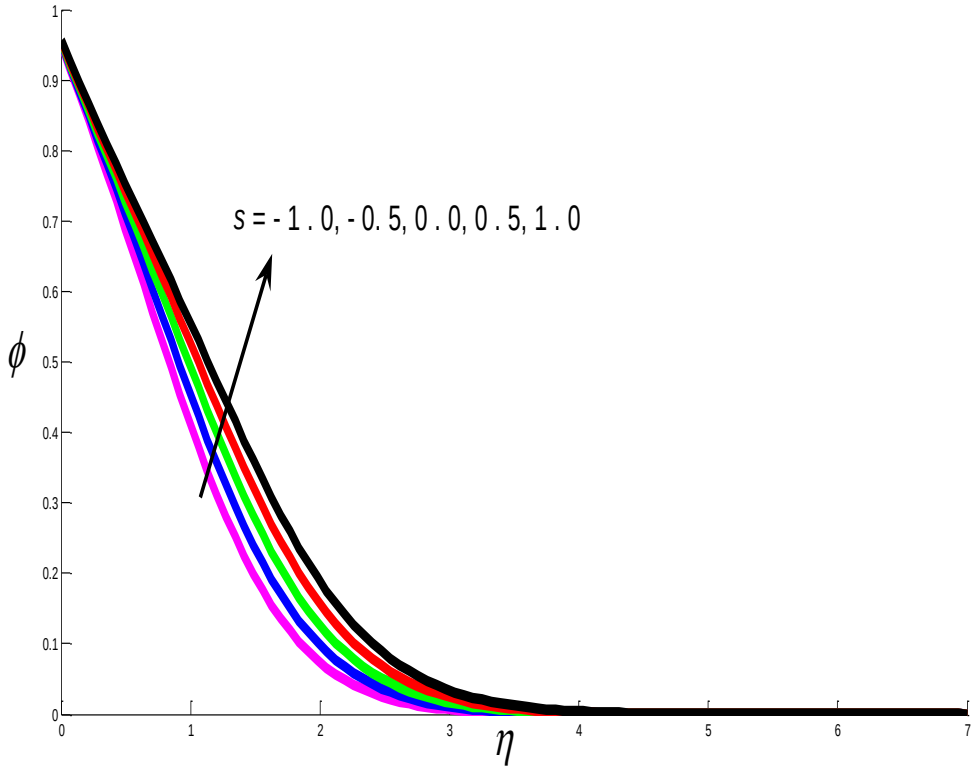

(d)

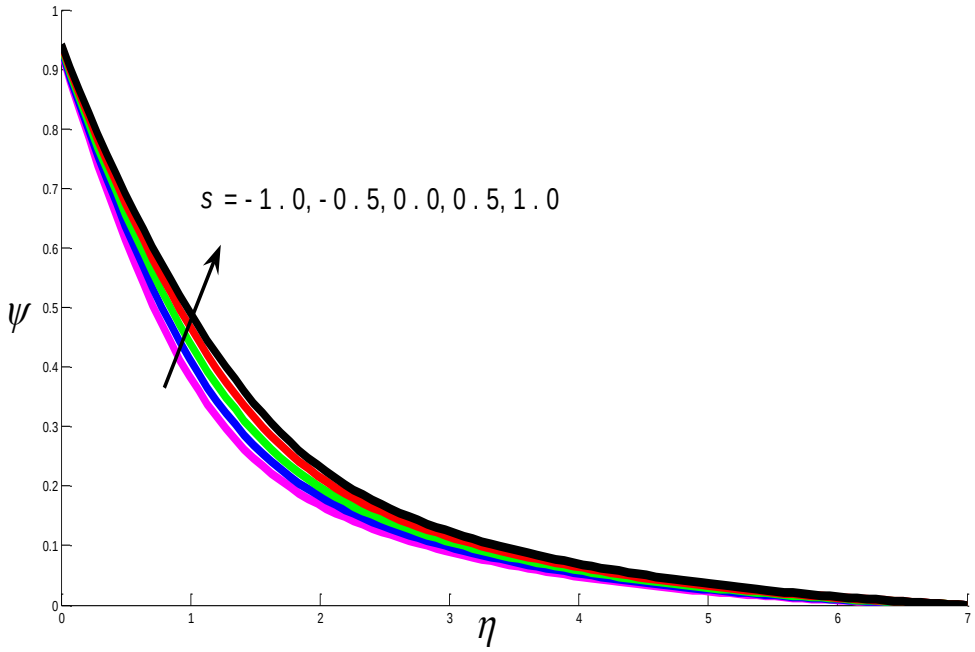

Figure 5 Profiles for different blowing parameter *s*

(a)

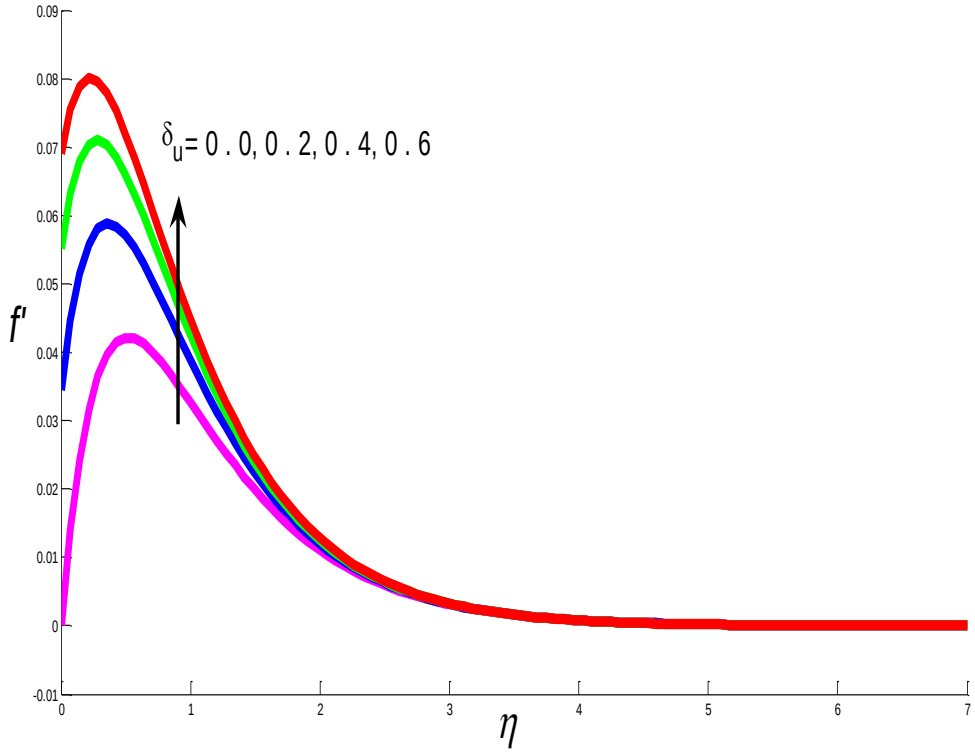

(b)

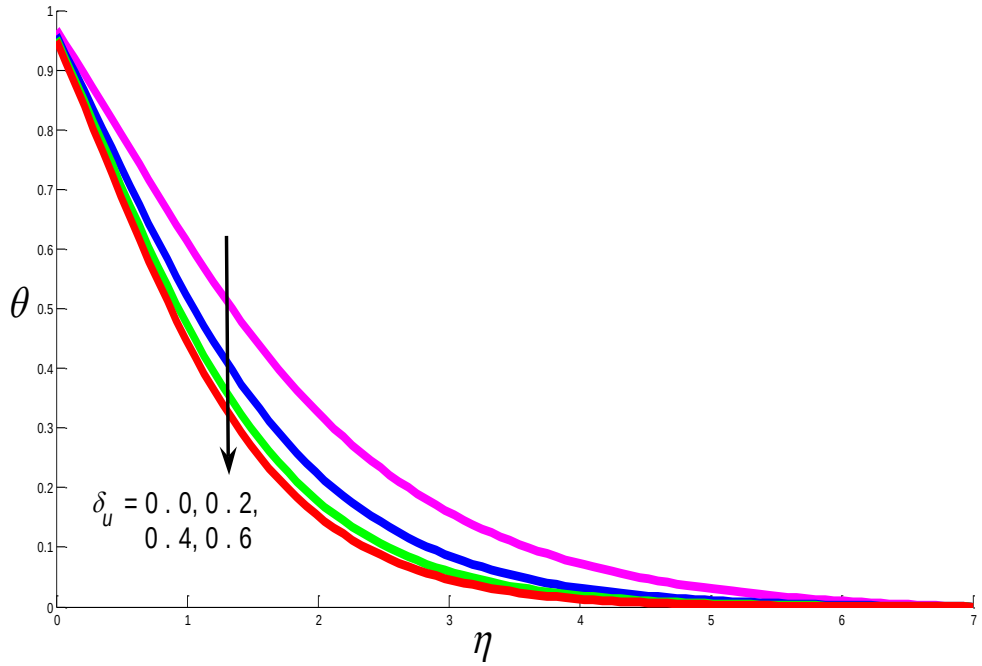

(c)

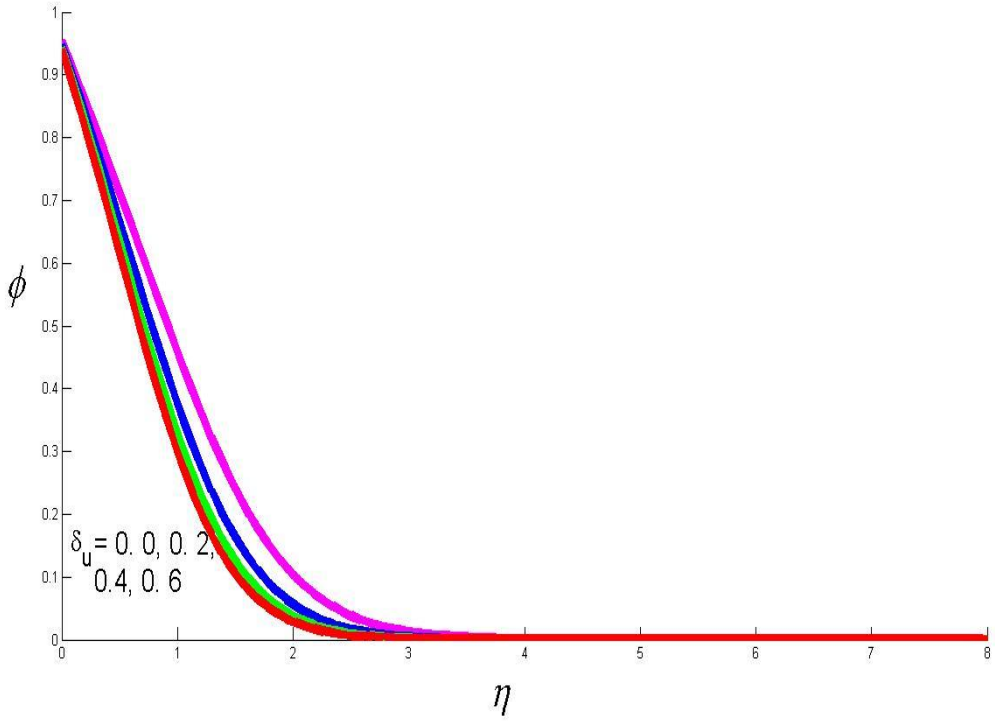

(d)

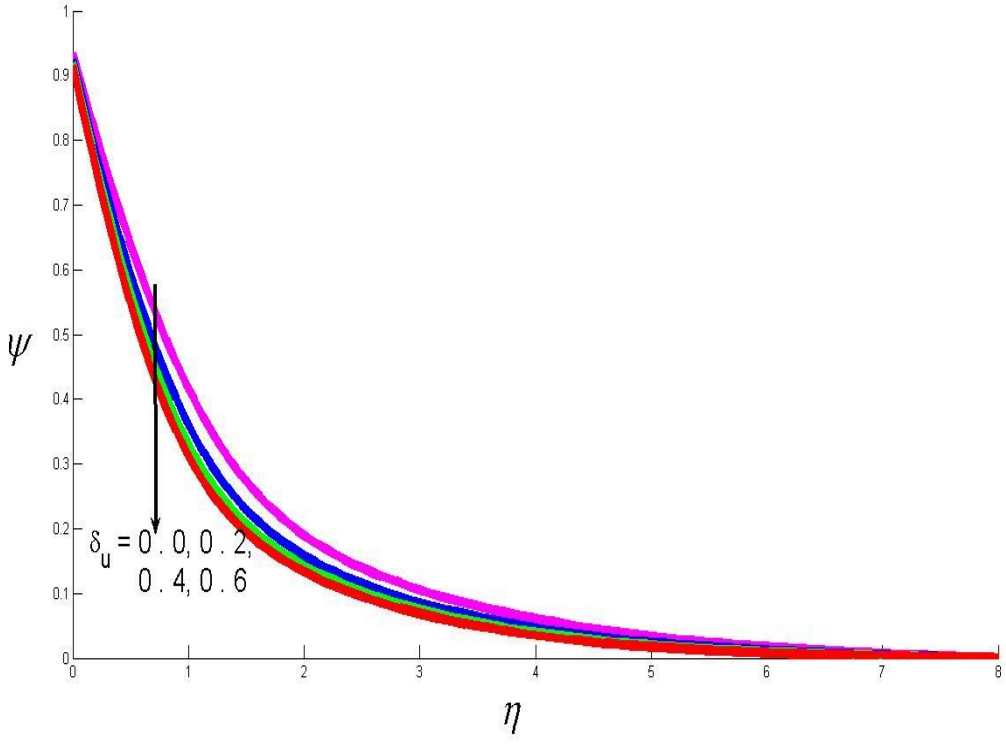

Figure 6 Profiles for different radial slip parameter δ_u

(a)

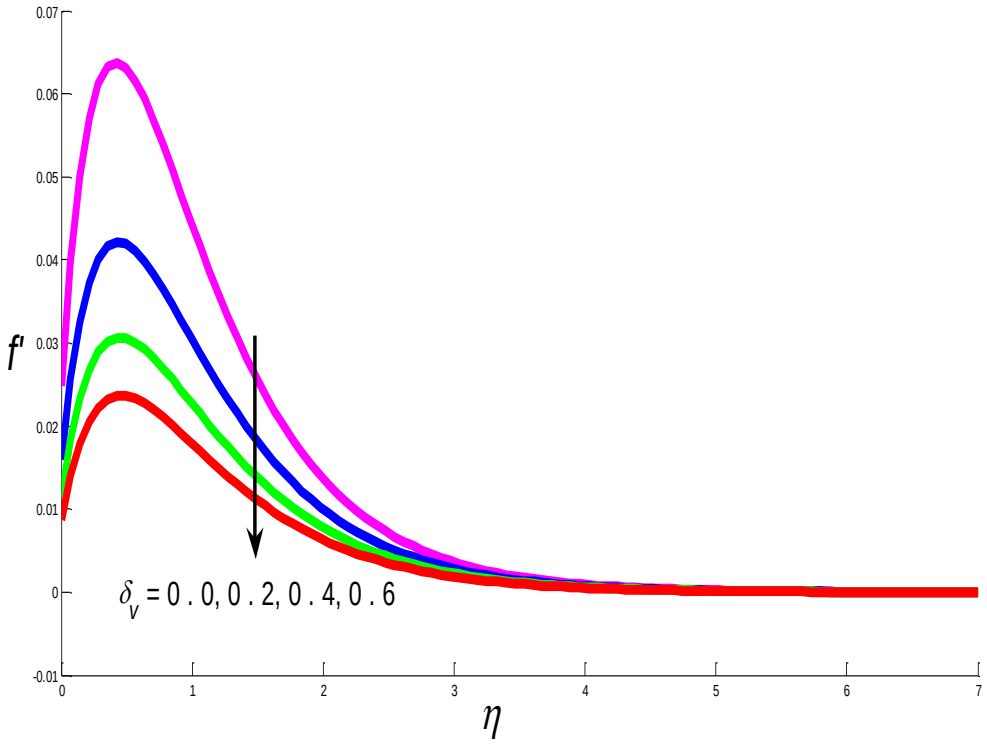

(b)

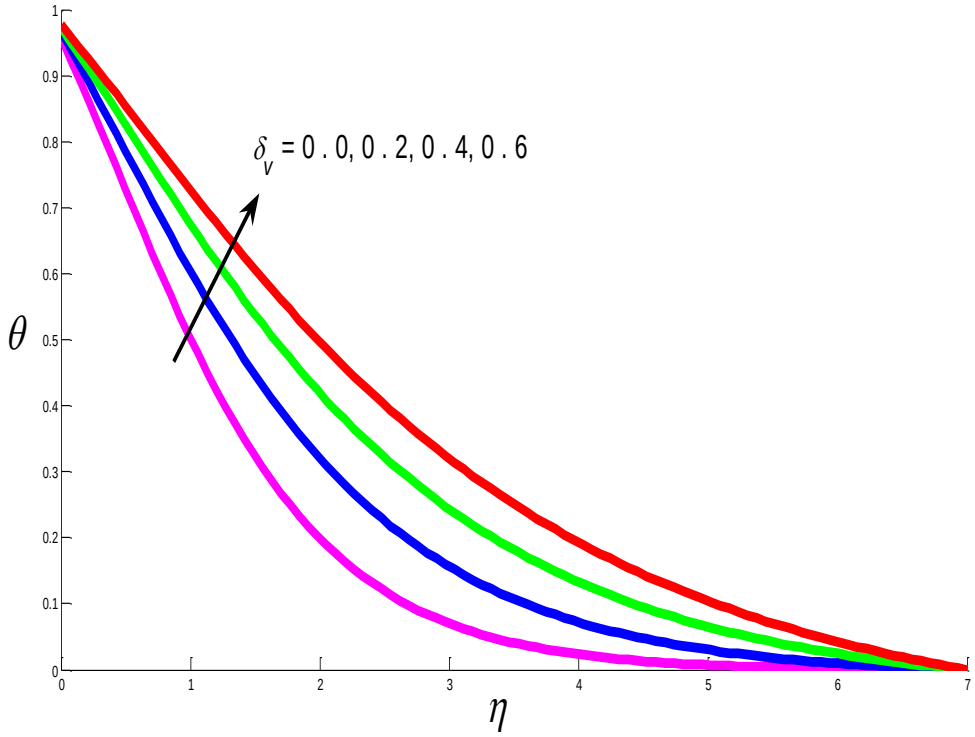

(c)

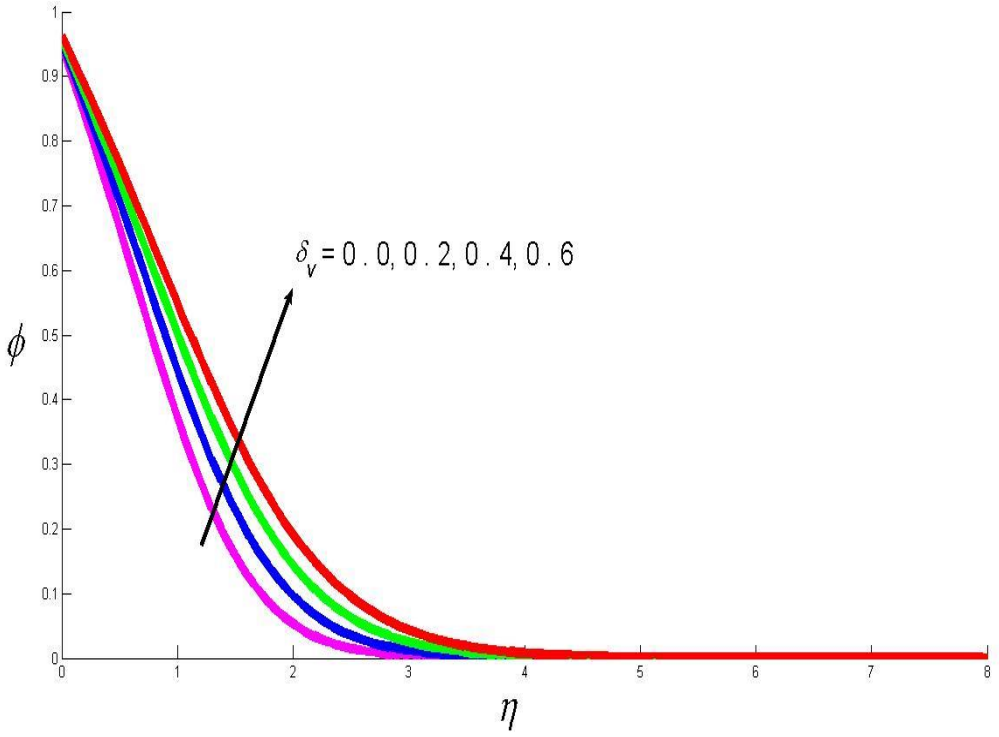

(d)

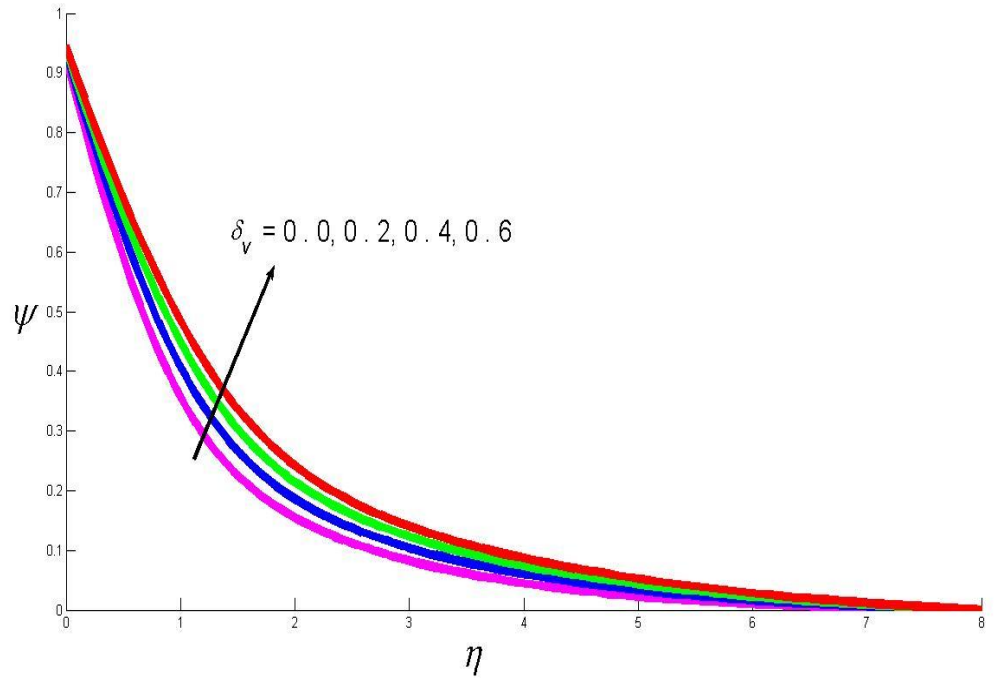

Figure 7 Profiles for different tangential slip parameter, δ_v

(a)

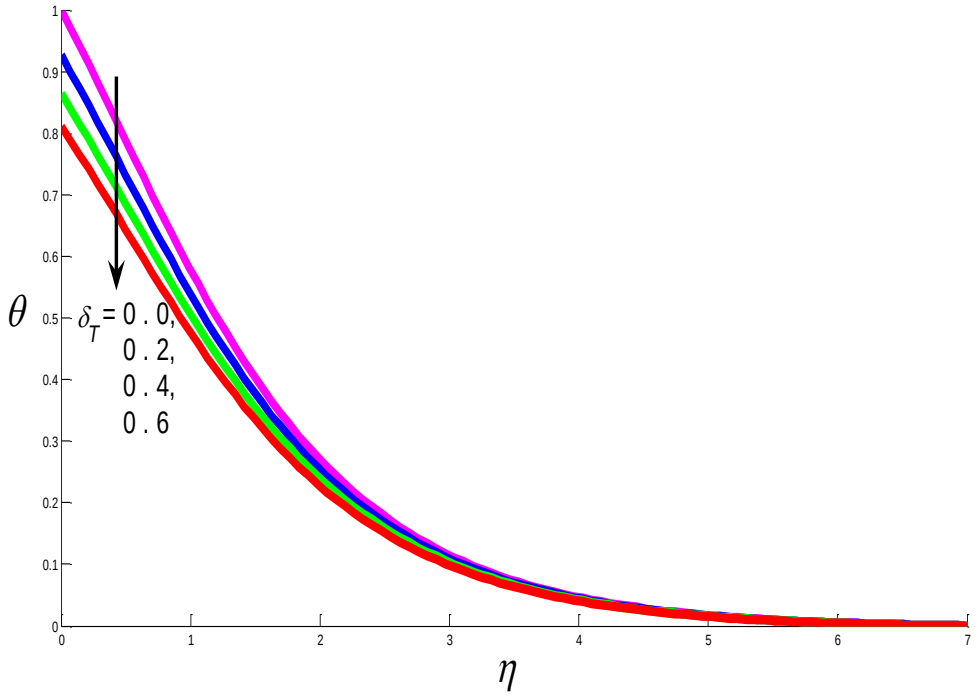

(b)

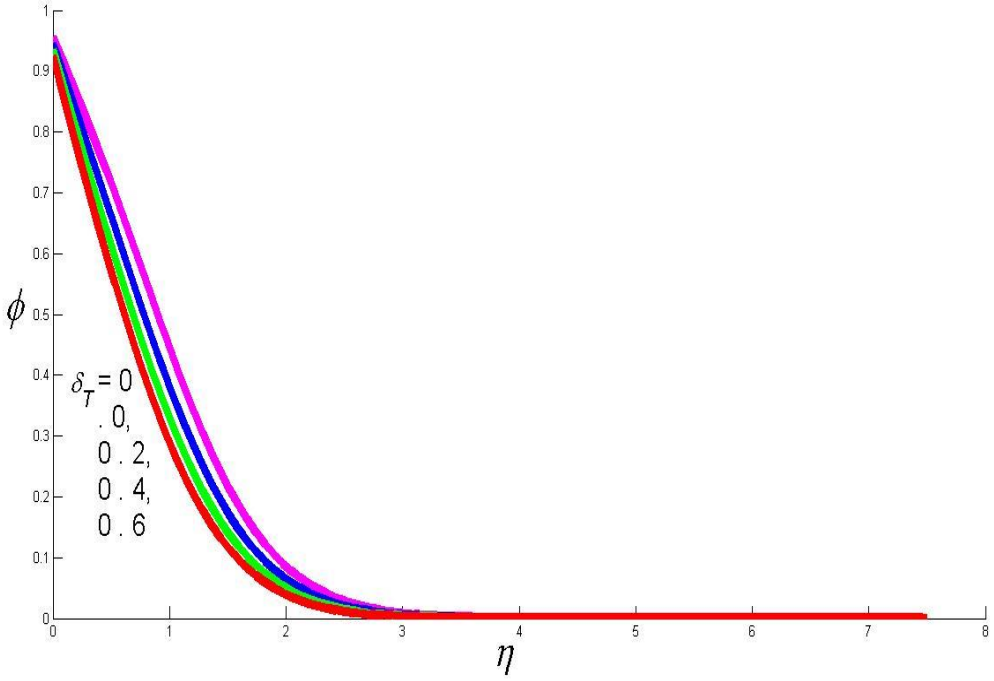

(c)

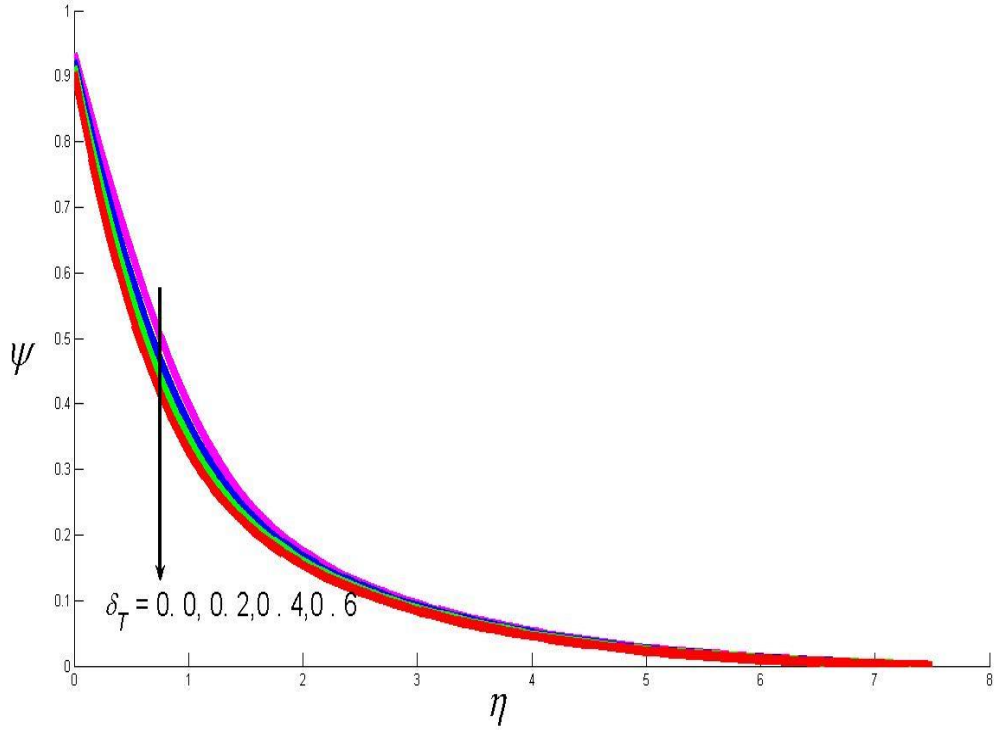

Figure 8. Profiles for different thermal jump (slip) parameter δ_T

(a)

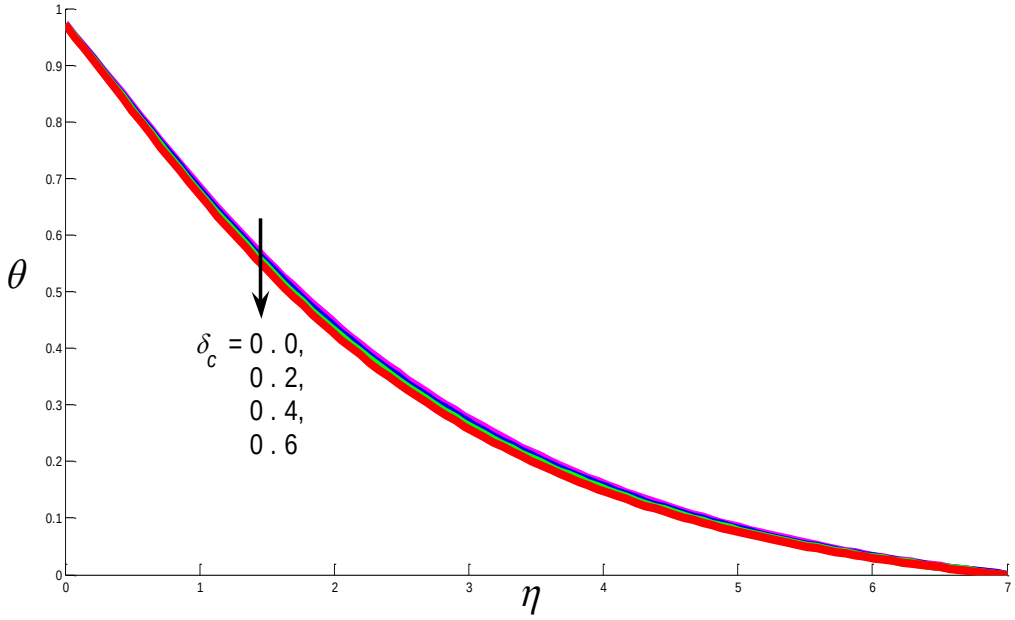

(b)

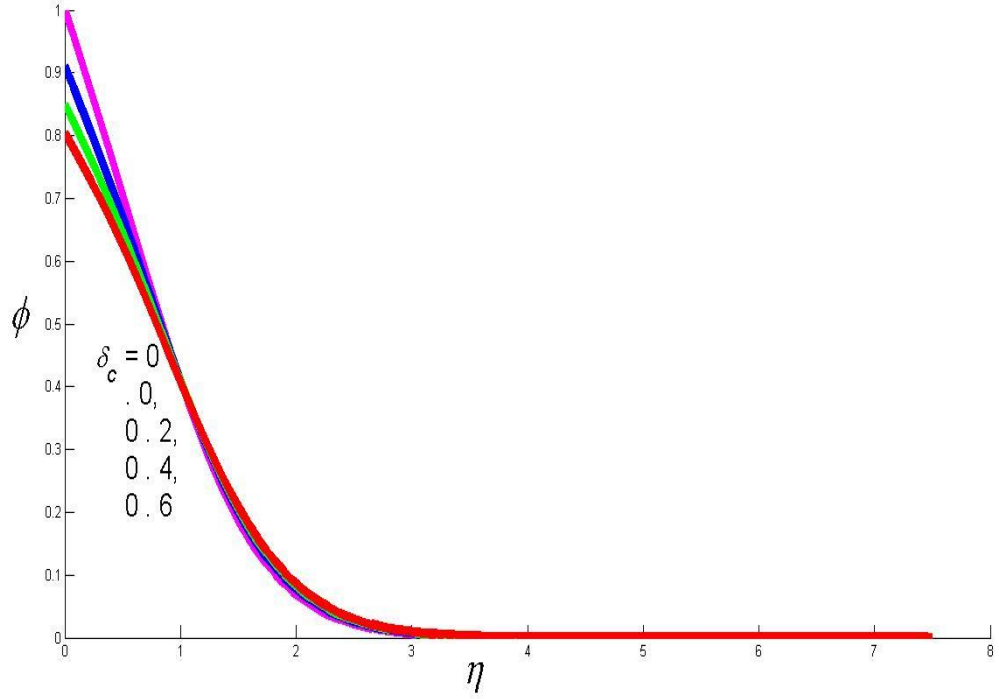

(c)

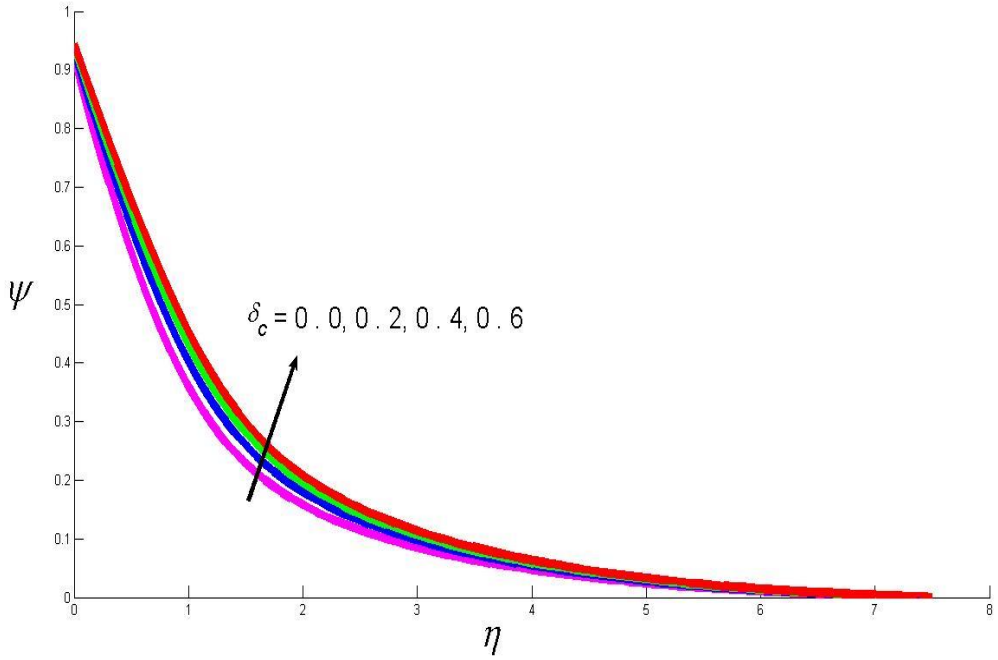

Figure 9 Profiles for different nanoparticle concentration slip parameter, δ_c

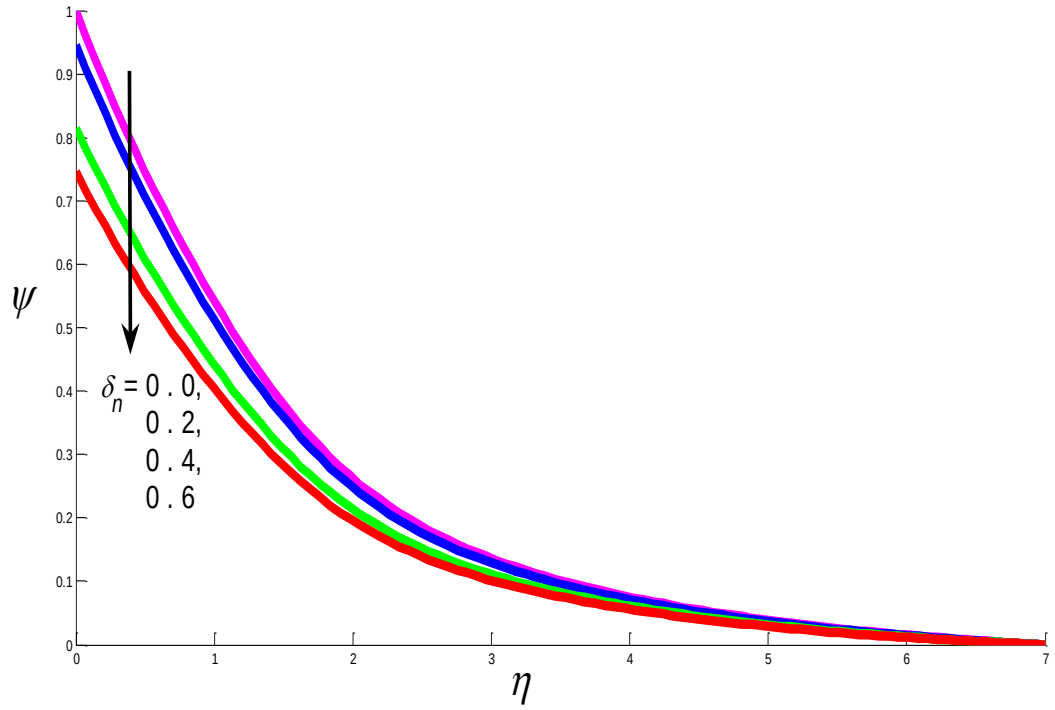

Figure 10. Profiles for different motile micro-organism slip parameter, δ_n

(a)

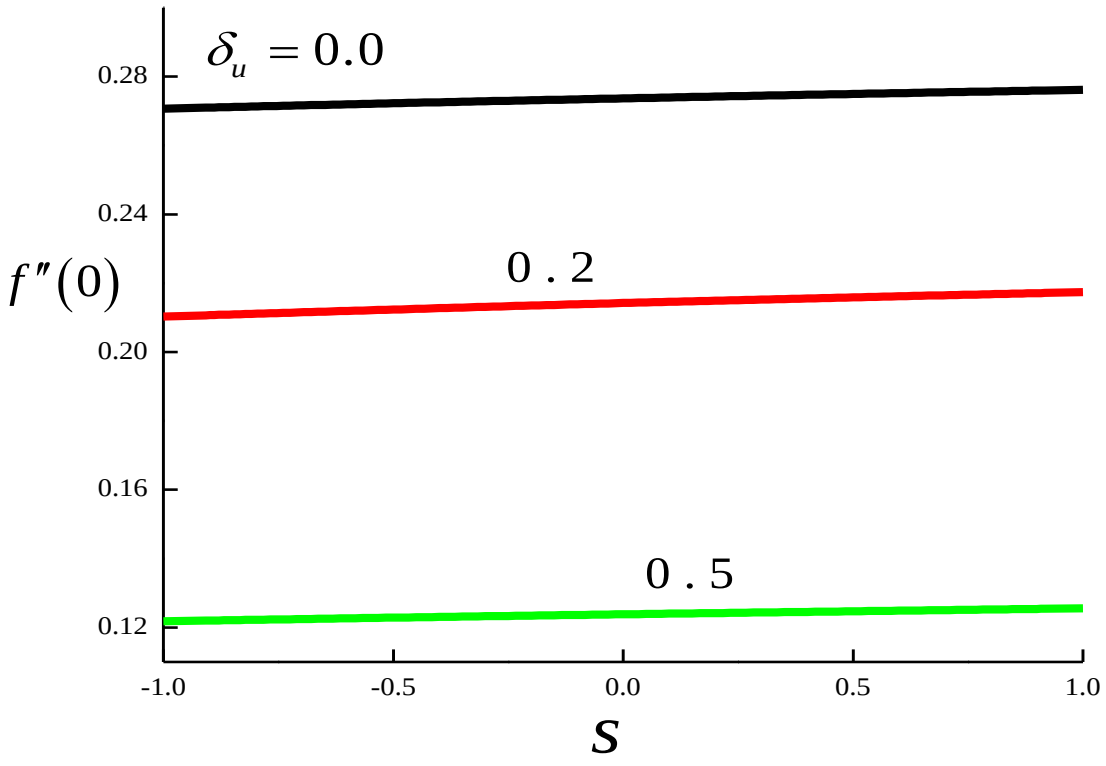

(b)

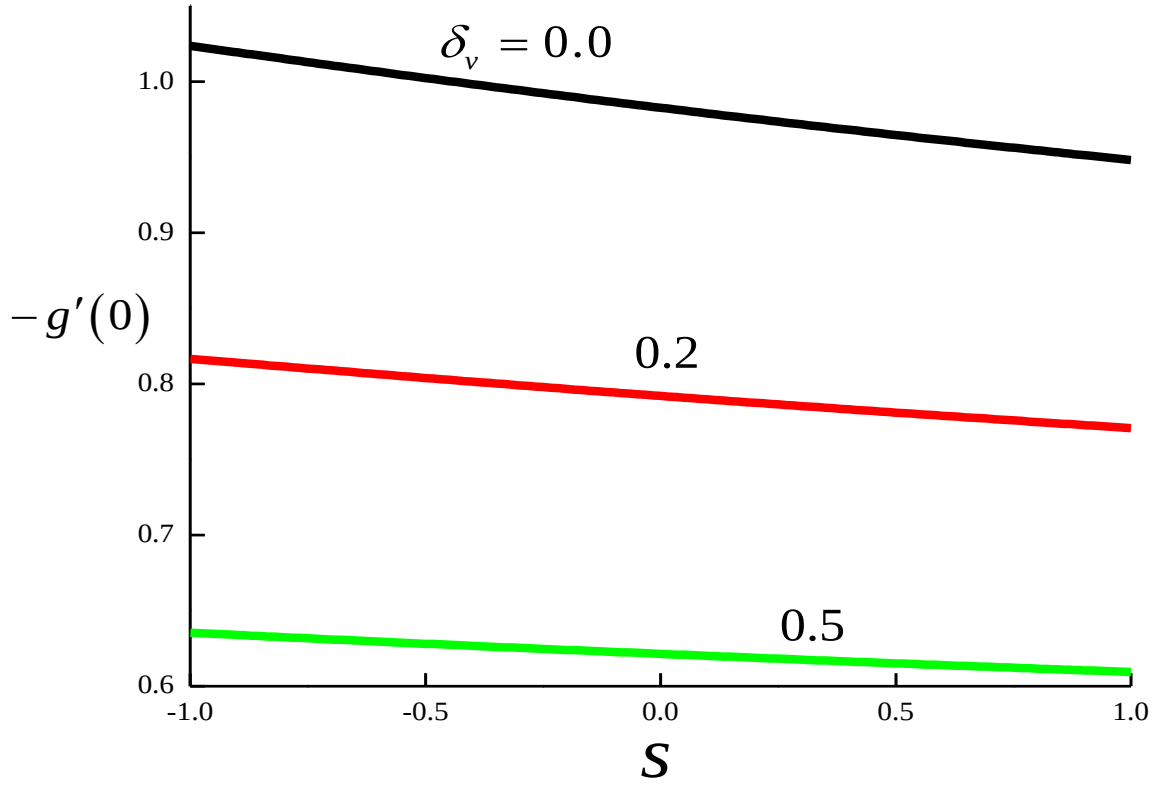
$\delta_v = 0.0$
0.2
0.5
$-g'(0)$
1.0
0.9
0.8
0.7
0.6
-1.0
-0.5
0.0
0.5
1.0
S

(c)

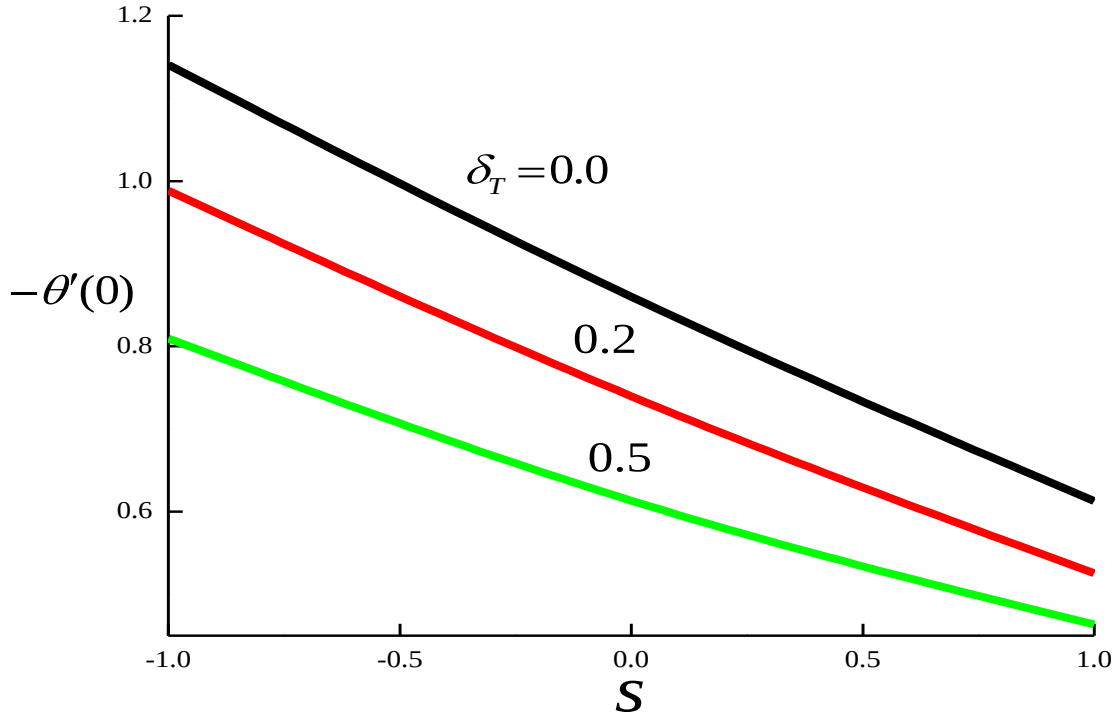
$\delta_T = 0.0$
0.2
0.5
$-\theta'(0)$
1.2
1.0
0.8
0.6
-1.0
-0.5
0.0
0.5
1.0
S

(d)

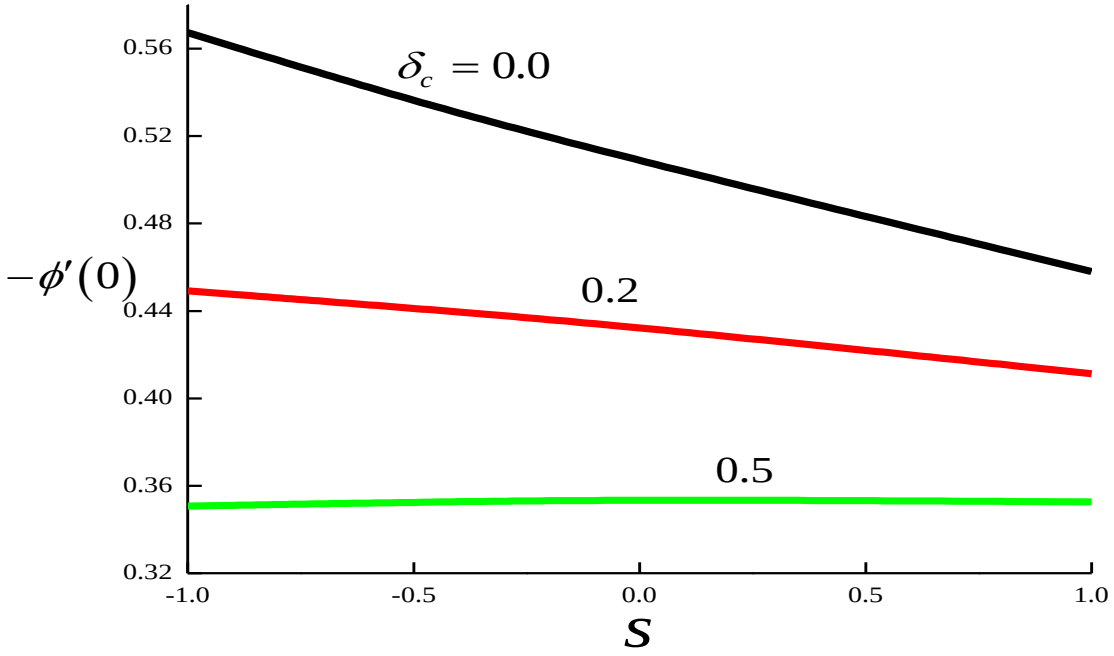

(e)

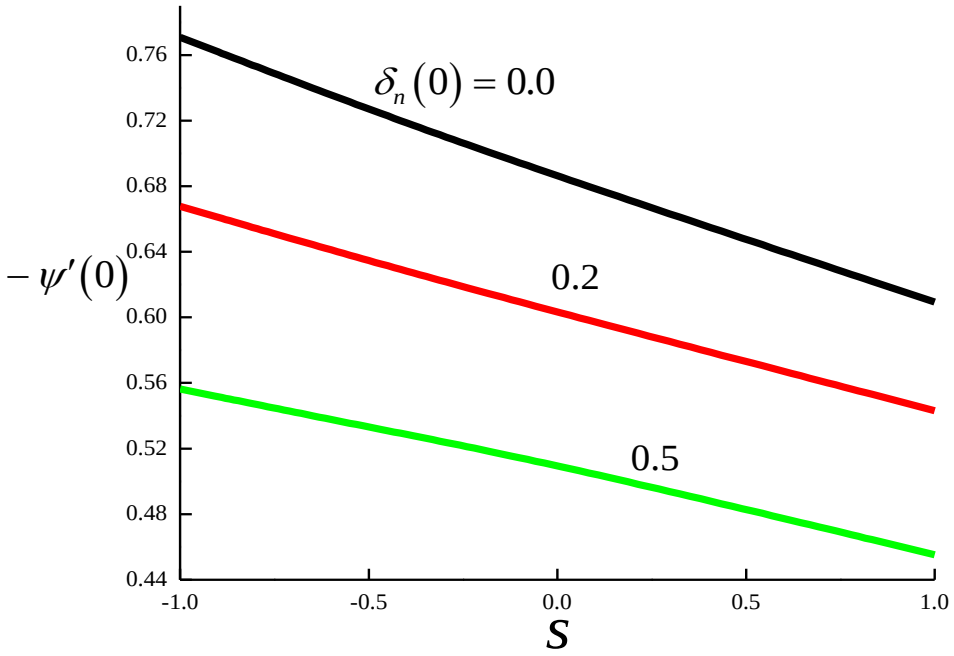

Figure 11 Impact of Stefan blowing parameter on $f''(0),\ -g'(0),\ -\theta'(0),\ -\phi'(0),\ -\psi'(0)$

5.1 Magnetic interaction parameter (M) effects

Figures 2a-d illustrate the impact of M i.e. magnetic interaction parameter (ratio of Lorentz magnetic body force and inertial rotational force), on f', θ, ϕ and ψ. The magnetic parameter arises

in both radial and tangential momentum equations (28) and (29). The Lorentz drag force is defined in the radial momentum as $-M\left(f'\right)$ and in the tangential momentum as $-M\left(g\right)$. Since a very weak effect is sustained by the tangential velocity it is not plotted. The dominant effect is on the radial flow. Both Lorentz forces are mutually orthogonal to the direction of the axial applied magnetic field i.e. they act parallel to the plane of the rotating disk. For $M=0$ the magnetic force vanishes, and electrically non-conducting flow is retrieved as considered in Bég *et al.* [52]. The present computations therefore apply to magnetohydrodynamic nanofluid rotating bioreactor systems, as elaborated in [39]. Radial velocity $\left(f'\right)$ profiles all ascend from the disk surface to peak near the surface and then descend smoothly to zero in the free stream. As M values are gained, the radial flow is quenched, and its peak is slowly displaced towards the disk surface. The Lorentzian drag therefore damps radial flow and increases momentum boundary layer thickness. Significant flow control is therefore achieved with stronger axial magnetic field. Maximum radial flow velocities correspond to the absence of magnetic field $\left(M=0\right)$ for which the hydrodynamic boundary layer thickness is lowest. Conversely temperature is greatly reinforced with larger values of M which is attributable to the supplementary work expended in dragging the nanofluid against the action of the axial magnetic field- this is dissipated as thermal energy and heats the boundary layer regime and also increases thermal boundary layer thickness. Strong elevation is observed therefore in temperatures in the swirling regime. Temperatures are therefore minimized for the non-conducting case $\left(M=0\right)$ as is thermal boundary layer thickness. Rapid convergence of solutions is achieved with MATLAB as observed from the sharp decay of all profiles to the free stream. Similarly, there is a considerable elevation in ϕ, and ψ by inflating M. As with temperature, the magnetic body force terms do not arise in the nanoparticle species or micro-organism species conservation boundary layer equations i.e. Eqns. (31) and (32). The coupling terms however between the radial momentum (Eqn. 28) i.e. radial velocity, and the temperature, nanoparticle and micro-organism equations enable the indirect effect of magnetic field on the other variables, and examples include $\Pr\left(2-m\right)f\,\theta'$ in Eqn. (30), $Le\,\Pr\left(2-m\right)f\,\phi'$ in Eqn. (31) and $Sb\left(2-m\right)f\,\psi'$ in Eqn. (32). Furthermore, supplementary linear and nonlinear terms also couple the temperature and micro-organism species fields e.g. $Nb\,\theta'\,\phi'$ in Eqn. (30), $+\frac{Nt}{Nb}\,\theta''$ in Eqn. (31) and $Pe\left(\psi'\,\phi'+\psi\,\phi''\right)$ in Eqn. (32). The implication is that there is a delicate interplay between all these variables. The increase in thermal diffusion mobilized by stronger magnetic field effect also encourages intensification in the nanoparticle diffusion and accelerates micro-organism species propulsion, leading to strong and sustained increase in their magnitudes throughout the boundary layer. Nanoparticle species boundary layer thickness and micro-organism species boundary layer thickness are therefore also boosted. The

presence of a magnetic field in the bioreactor swirling regime is therefore immensely beneficial to increasing thermal diffusion, nanoparticle motion and micro-organism swimming, all of which may then be optimized in actual designs [39].

5.2 Influence of Hall current parameter (m)

Figure 3a-d visualize the influence of Hall current parameter, m on profiles of f', θ, ϕ and ψ versus axial coordinate, η. As with the magnetic interaction parameter, M, the Hall parameter features only in the radial and tangential moment boundary layer Eqns. (28), (29), respectively in the terms, $-M\left(f'-h\,g\right)$ in the former and $-M\left(g+h\,f'\right)$ in the latter. Clearly the Hall terms exhibit the crossflow nature of the Hall current effect and both terms are coupled with magnetic interaction parameter, M. The Hall current effect describes the charge separation phenomenon in a conductive object (in this case the magnetized nanofluid) moving in a magnetic field. This charge separation is produced by the opposing Lorentz forces on the positive and negative charges, and leads to an externally detectable voltage, the Hall voltage, as noted by Bég et al. [45] and Cramer and Pai [55]. The Hall voltage amplitude is determined by the strength of the Lorentz force and the charge density and mobility, as reflected in the appropriate terms in Eqns. (28, 29). The Lorentz force is proportional to the magnetic field B_0 and the velocity of motion $\left(f'g\right)$, while the charge density and mobility are characterized by the overall conductivity σ of the object, including the dielectric contribution. Thus, a significant Hall voltage is created which is directly proportional to the product of electrical conductivity, radial (or tangential) velocity and axial magnetic field. Intensification in Hall parameter therefore induces a significant acceleration in the radial flow (Fig. 3a). However, unlike magnetic parameter, M, it does not induce a displacement in the peak radial velocity from the disk surface. For all Hall parameter values, and indeed even in the absence of Hall current $\left(h=0\right)$ the peak velocity location is fixed at a short distance from the disk surface. However, momentum boundary layer thickness is reduced with increasing Hall parameter, h, which is the opposite effect to that induced with stronger magnetic interaction parameter, M. There is a slight overlap in profiles further into the free stream where the Hall current is found to produce weak radial flow deceleration. However, the dominant effect for the boundary layer regime is strong acceleration with greater Hall effect. The combined effect of axial magnetic field and Hall current may therefore be exploited to significantly manipulate the radial flow in the regime which allows bioreactor designers further flexibility in options. Increasing Hall parameter also results in a reduction in θ (Fig. 3b) and again this is the opposite trend to that computed with increasing magnetic parameter, M (Fig. 2b). This concurs with many other investigations on Hall magnetohydrodynamics e. g. Khan *et al.* [44], [46], and has also been identified by Hughes and Young [27]. Therefore, while stronger magnetic field induces heating in the boundary layer regime, greater Hall current produces a

cooling effect and decreases thermal boundary layer thickness. A marked *depletion* in ϕ and ψ also accompanies an increment in Hall current parameter, h, as observed in Figs. 3c, d. Again, this is the reverse behavior to that computed with increasing magnetic field parameter, *M*. The crossflow Hall voltage therefore depletes nanoparticle and gyrotactic micro-organism species boundary layer thicknesses. It is interesting to also note that the nanoparticle profiles (ϕ) decay to the free stream zero value faster from the disk surface compared with the micro-organism density (ψ) and this is inevitably related to the difference in species diffusivities relative to momentum diffusivity.

5.3 Influence of Darcy parameter (Da)

Figures 4a-d depict the distributions of f', θ, ϕ and ψ for various Darcy numbers (Da). Darcy number arises in the Darcian linear impedance body force terms, $-\frac{1}{Da} f'$ in the radial momentum Eqn. (28) and $-\frac{1}{Da} g$ in the tangential momentum Eqn. (29). The porous medium is isotropic and therefore only a single Darcy number is required to simulate permeability effects. Large values of Darcy number are employed since high permeability is required in rotating bioreactor designs [23-26]. There is a strong acceleration in radial flow (Fig. 4a) with increment in Darcy number, since the radial Darcy impedance term is reduced i.e. porous media drag is depleted. Lower Darcy number corresponds to lower permeability which inhibits the radial flow and vice versa for higher Darcy number. In computational tests the impact on tangential velocity distribution was found to negligible and therefore the tangential velocity plot is omitted. Of course, the Darcy model is restricted to low Reynolds number viscous dominated flows and the rotational velocity of the bioreactor is therefore relatively low. For higher spin velocity of the disk, inertial effects will be invoked, and a Forchheimer second order drag arises. Although this has not been considered in the present study, since attention is confined to slow rotation in the magnetic bioreactor, future investigations may consider Darcy-Forchheimer models for the porous medium [64]. Momentum boundary layer thickness is reduced with greater Darcy number. There is also a progressive shift in peak velocity location further from the disk surface with increasing Darcy number. Fig. 4b shows that a considerable depletion in temperature is generated with increment in Darcy number. Higher Darcy number implies a progressive depletion in solid matrix fibers in the porous medium adjacent to the rotating disk. This suppresses thermal conduction in the regime and reduces temperature of the magnetized nanofluid i. e. a cooling effect is induced for more permeable media. Thermal boundary layer thickness is therefore also reduced, and the trend is sustained at any and all locations transverse to the disk surface. Significant depletion in ϕ and ψ magnitudes is also computed with greater Darcy number, as visualized in Figs. 4c, d, respectively. Less permeable media (lower Darcy

number) with greater solid fiber presence are therefore found to encourage nanoparticle diffusion and micro-organism propulsion in the rotating bioreactor regime, and also result in greater nanoparticle and micro-organism species boundary layer thicknesses. Greater permeability i.e. the decrease in solid fibers and greater percolation of nanofluid actually inhibits nanoparticle mass diffusion and retards the micro-organism propulsion. The presence of a high permeability porous medium, therefore, while beneficial to damping the radial flow and achieving enhanced flow regulation, is counter-productive for the transport of heat, nanoparticles and micro-organisms.

5.4 Influence of Stefan blowing parameter (s)

Figure 5a-d illustrates the evolution in f', θ, ϕ and ψ for various Stefan blowing parameter values, s. The parameter $s = \Delta C\left(1 - C_w\right)$, as defined in Eqn. (35) and features in the wall (disk surface) boundary condition, $f'(0) = \dfrac{s}{Le\ \mathrm{Pr}\left(2 - m\right)}\phi'(0)$, in Eqn. (33). It therefore involves the dimensional nanoparticle concentration field, C. It does not arise in the free stream boundary conditions. Stefan blowing is distinct from the conventional wall mass flux (transpiration) effect used in boundary layer flows which relates to the suction/injection generated by perforations on the disk surface. Figure 5(a) indicates that radial velocity is suppressed (deceleration) with increasingly strong suction i.e. negative Stefan blowing $(s < 0)$ whereas radial acceleration is significantly accentuated for strong blowing $(s > 0)$. Momentum boundary layer thickness is therefore elevated with suction and depleted with Stefan blowing in the swirl regime. Stefan blowing therefore strong aids the radial momentum diffusion whereas suction counteracts diffusion. For the case where Stefan blowing is neglected $(s = 0)$, the radial velocity profile is intercalated between the Stefan blowing and reverse Stefan blowing (suction) cases. Backflow or separation is however never initiated with suction despite the strong retarding effect. Inclusion of the Stefan blowing hydrodynamic effect may therefore be exploited in spinning bioreactor designs [17-22] since it provides a facility for adjusting the mass flux from the potential flow which in turn can be deployed to regulate radial velocity distribution. This may also be very useful in producing more homogenous coatings in Thiobacillus ferrooxidans biofilm deposition processes in spinning bioreactors [25]. The inclusion of spherical nanoparticles [65] and gyrotactic micro-organisms which do not interact also achieves a stable regime. Figs. 5b, c, d similarly demonstrate that with increased Stefan blowing the temperature (Fig. 5b), nanoparticle concentration (Fig. 5c) and micro-organism density number (Fig. 5d) are all boosted i.e. with stronger mass flux from the spinning disk surface to the potential flow, thermal diffusion, nanoparticle migration and micro-organism propulsion in the swirling regime are all assisted. Thermal, nanoparticle concentration and micro-organism boundary layer thicknesses are

therefore all enhanced with s. The opposite effect is instigated with greater suction (reverse Stefan blowing).

5.5 Influence of radial momentum (hydrodynamic) slip parameter (δ_u)

Fig.6 (a)-(d) present the impact of radial momentum (hydrodynamic) slip parameter (δ_u) on f', θ, ϕ and ψ. This parameter arises in the disk surface (wall) boundary condition, $f'(0) = \delta_u \; f''(0)$. A strong expedition in the radial flow (Fig. 6a) is induced with increment in radial slip parameter, in particular near the disk surface. The velocity peak is also displaced closer to the wall with greater radial slip. Radial velocity is therefore minimized in the absence of radial slip. The implication is that neglection of the slip effect leads to an under-estimate in the actual radial velocity. Slip is known to be significant in rotating bioreactors as noted in Lawrence et al. [66] as are porous media effects, considered in earlier graphs. Conversely there is a strong decrement induced in temperature (Fig. 6b), nanoparticle concentration (Fig. 6c) and microorganism density number (Fig. 6d) values with increment in higher radial slip value, δ_u. Strong cooling and inhibition of nanoparticle diffusion and micro-organism propulsion is therefore induced with greater radial momentum slip effect. Thermal boundary layer, nanoparticle species boundary layer and micro-organism boundary layer thicknesses are therefore significantly reduced with greater radial slip, whereas the momentum boundary layer thickness is reduced. The inclusion of the radial slip parameter is therefore important in more realistic models of rotating bioreactors since when it is absent the radial velocity is under-predicted and the temperature, nanoparticle concentration and microorganism density number magnitudes are over-estimated. Asymptotically smooth convergence is achieved in the free stream with all profiles confirming the prescription of an adequately large infinity boundary condition in the MATLAB bvp4c computations.

5.6 Influence of tangential (circumferential) momentum slip parameter (δ_v)

Figs. 7 (a)-(b) present the impact of tangential (circumferential) momentum slip parameter (δ_v) on the f', θ, ϕ and ψ. This parameter features also in the disk surface (wall) boundary condition for the tangential velocity i.e. $g(0) = 1 + \delta_v \; g'(0)$. Converse to the radial momentum slip effect, an increment in tangential slip produces marked deceleration in the radial flow (Fig. 7a). The radial and momentum fields are strongly coupled via the terms, $+ g^2$ and $- M \left(f' - h \, g \right)$ in the former Eqn. (28) and the terms $+ (2 - m) f \; g', \; - (2 - 2m) f' g, \; - M \left(g + h \; f' \right)$ in the latter Eqn. (29). The primary flow is in the radial direction because the disk is stretched radially. Hence for larger tangential slip, hydrodynamic boundary layer thickness is escalated. There is a also a weak

migration in the peak radial velocity towards the disk surface (wall) with greater tangential slip effect. Evidently in the absence of tangential slip, radial velocity is maximized. In other words, radial velocity is over-predicted in the swirling regime when tangential slip is neglected (as opposed to being under-predicted when radial momentum slip is ignored). Contrary to the radial slip effect, increasing tangential slip results in a significant enhancement in the temperature (Fig. 7b), nanoparticle concentration (Fig. 7c) and microorganism density number (Fig. 7d) magnitudes. All the associated boundary layer thicknesses are therefore elevated with greater tangential slip. Micro-organism propulsion is exacerbated with greater tangential slip as is the heating of the regime and the diffusion of the magnetized nanoparticles. Both figures 6 and 7 confirm that the inclusion of anisotropic momentum slip adds a new level of sophistication to modelling of rotating bioreactors and exert tangible effects on the radial velocity distribution and other transport characteristics.

5.7 Influence of thermal slip (jump) parameter, δ_T.

Figures 8(a)-(c) visualize the profiles for temperature, nanoparticle concentration and motile micro-organism density number with various values of thermal slip (jump) parameter, δ_T. The thermal slip parameter do not show any major changes on the radial velocity and hence not shown pictorially. The thermal slip parameter, δ_T appears again in the disk surface (wall) boundary condition, $\theta(0) = 1 + \delta_T \; \theta'(0)$ and produces a step change in the temperature ("temperature jump") at the wall. This decreases temperature diffusion from the wall to the magnetic but only weakly accelerates the radial flow (Fig. 8a) and a meager reduction in momentum boundary layer thickness. A strong decrease in temperature is however computed with greater thermal slip (Fig. 8b), and is pronounced at the disk surface, decaying in magnitude with progressive distance further into the boundary layer transverse to the disk surface. Thermal boundary layer thickness is therefore considerably reduced with stronger thermal slip. Maximum temperatures are computed in the absence of thermal slip again emphasizing that the neglecting of thermal slip produces an over-estimate in the temperature distribution in the swirling regime. A weaker decrease in ϕ (Fig. 8c) and ψ (Fig. 8d) is computed with elevation in thermal slip parameter. Nanoparticle and microorganism species boundary layer thicknesses are therefore marginally reduced.

5.8 Influence of nanoparticle concentration slip parameter, δ_c. f', θ, ϕ

Figures 9a-c present the distributions for θ, ϕ and ψ on nanoparticle concentration slip parameter, δ_c. As with the other slip parameters, nanoparticle concentration slip parameter is present in the wall boundary condition, $\phi(0)\,1 + \delta_c \; \phi'(0)$ in Eqn. (33). Increasing δ_c does not influence substantially the radial flow f' and hence not shown in the form of figure. Larger δ_c also produces

a relatively weak decrement in the temperature magnitudes (Fig. 9b). However, it strongly reduces the nanoparticle concentration magnitudes at the disk and for some distance into the boundary layer. Conversely there is a minor uplift in ψ with increasing nanoparticle mass slip effect. These trends are sustained at all values of the axial coordinate, η. Transport of nanoparticles from the disk surface to the swirling boundary layer flow is evidently stifled with the nanoparticle mass slip effect, and the coupling terms (explained earlier) also result in non-trivial modifications in the other transport characteristics. Overall, the momentum and micro-organisms boundary layer thicknesses are increased whereas the nanoparticle and gyrotactic micro-organism boundary layer thicknesses are upsurged with larger nanoparticle slip effect.

5.9 Influence of microorganism slip parameter δ_n

Figure 10 depict the influence of microorganism slip parameter δ_n on ψ. f', θ, ϕ and ψ. Almost negligible modification is computed for the radial velocity f', temperature θ and nanoparticle concentration ϕ with a large increment in the δ_n values and hence not shown graphically. The micro-organism slip parameter which arises in the surface (wall) boundary condition $\psi(0) = 1 + \delta_n \psi'(0)$ in Eqn. (33) does not therefore influence the other transport characteristics. However, it induces a substantial depletion in microorganism density number magnitudes (Fig. 10). There is a substantial step difference at the disk surface in microorganism density number which inhibits the propulsion of micro-organisms from the wall into the rotating disk boundary layer regime. There is therefore effectively a notable decrease in micro-organism species boundary layer thickness with increasing micro-organism slip effect but no tangible alteration in the momentum, nanoparticle concentration or thermal boundary layer thicknesses.

5.10 Influence of Stefan blowing and different slip parameters on disk surface gradients

Radial skin friction (Fig. 11a) is considerably reduced with increasing radial slip parameter, δ_u, but weakly enhanced with Stefan blowing i.e. $s > 0$ (and weakly decreased with reverse Stefan blowing i.e. $s < 0$). Tangential skin friction (Fig. 11a) is also markedly depleted with increasing tangential (circumferential) slip parameter, δ_v, but weakly reduced with Stefan blowing i.e. $s > 0$ but weakly increased with reverse Stefan blowing i.e. $s < 0$ (suction). In all cases the profiles are approximately linear in nature. Generally maximum radial and tangential skin friction therefore correspond to the absence of anisotropic slip effects. Nusselt number is very strongly reduced with increasing Stefan blowing (Fig. 11c) and greater thermal slip, δ_T, but considerably enhanced with reverse Stefan blowing. With increasing nanoparticle mass slip, δ_c there is a significant reduction in nanoparticle

Sherwood number (Fig. 11d). At lower values of nanoparticle slip $(\delta_c = 0, 0.2)$ there is also a decrease in Sherwood number magnitudes for greater Stefan blowing and an increase with reverse Stefan blowing; however, at the highest value of $\delta_c = 0.5$ the Stefan blowing parameter exerts the opposite effect. The diffusion of nanoparticles from the boundary layer swirling regime to the disk surface is therefore very sensitive to Stefan blowing and slip effects, which can be exploited to control nanoparticle distributions in bioreactor designs. Increasing Stefan blowing effect $(s > 0)$ and stronger motile micro-organism slip consistently suppress the gyrotactic micro-organism density gradient at the disk surface (Fig. 11e) whereas reverse Stefan blowing ($s < 0$ i.e. suction) induces the converse trend. The implication is that with stronger Stefan blowing, the motile micro-organisms are discouraged from moving from the boundary layer to the disk surface whereas the contrary effect is induced with reversed Stefan blowing.

6. CONCLUSIONS

The present study has been inspired by new trends in magnetohydrodynamic spinning nanotechnological bioreactor designs in which nutrients may be better distributed in porous media. A theoretical and computational analysis has therefore been conducted for steady swirling Von Karman flow from a rotating disk bioreactor to a porous medium saturated with a magnetic nanofluid containing gyrotactic micro-organisms. An axial magnetic field perpendicular to the disk with Hall currents has been considered in order to provide extra mechanisms of control for the swirling boundary layer flow regime. The disk has been assumed to stretching the radial direction with a power-law velocity. The Buongiorno nanoscale, Kuznetsov bioconvection and Darcy porous media models have been utilized and additionally anisotropic momentum, thermal, nanoparticle concentration and motile micro-organism slip effects incorporated. Stefan blowing has been simulated via an appropriate surface boundary condition. The transformed nonlinear ordinary differential boundary value problem subject to physically realistic boundary conditions has been solved with MATLAB bvp4c shooting quadrature Verification with earlier solutions for the non-magnetic Von Karman bioconvection nanofluid case has been included and additional validation of the general magnetic model performed with the Adomian decomposition method (ADM). The main conclusions of the present simulations may be summarized as follows:

-Strong radial flow deceleration is induced with greater magnetic field whereas θ, ϕ and ψ are significantly enhanced in the swirling flow regime.

-Radial flow is boosted markedly with greater Hall current effect whereas the θ, ϕ and ψ magnitudes are suppressed.

-With elevation in Darcy number (dimensionless permeability parameter) there is a considerable acceleration in radial flow but a strong decrease in temperature, nanoparticle concentration and motile micro-organism density number.

-With greater Stefan blowing effects, all transport characteristics i.e. f', θ, ϕ and ψ are enhanced.

-The contrary behavior is computed with reverse Stefan blowing (suction).

-With greater radial momentum slip effect and thermal slip effect, radial velocity is elevated whereas the temperature, nanoparticle concentration and motile micro-organism number density are substantially depleted.

-With greater tangential momentum slip effect, radial velocity is reduced whereas the temperature, nanoparticle concentration and motile micro-organism number density are markedly enhanced.

-With greater nanoparticle mass slip effect, motile micro-organism number density is enhanced whereas the radial velocity, temperature, nanoparticle concentration are significantly decreased.

-With greater gyrotactic micro-organism slip effect, motile micro-organism number density is considerably depressed whereas there is no tangible modification in radial velocity, temperature or nanoparticle concentration.

-Radial skin friction is decreased with increasing radial slip parameter, weakly enhanced with Stefan blowing and weakly decreased with reverse Stefan blowing (suction). Tangential skin friction is also strongly reduced with increasing tangential (circumferential) slip parameter, weakly reduced with Stefan blowing but slightly increased with reverse Stefan blowing.

-Nusselt number is significantly decreased with increasing Stefan blowing and higher values of thermal slip, whereas it is enhanced with reverse Stefan blowing.

-Nanoparticle Sherwood number is markedly depleted with increasing nanoparticle mass slip.

-Gyrotactic micro-organism density gradient at the disk surface i.e. micro-organism mass transfer rate is suppressed with increasing Stefan blowing effect and stronger motile micro-organism slip whereas reverse Stefan blowing (suction) generates the opposite behavior.

-MATLAB bvp4c and Adomian decomposition have been found to be very versatile numerical approaches for studying hybrid magnetic rotating nanofluid bioreactor swirl dynamics. However only Newtonian flow has been considered. Future studies may extend the formulation to include more complex rheological effects with e. g. Eringen's micropolar model [67], which may provide a good framework for rotational micro-spin of nanofluid particles. Efforts in this direction will be communicated imminently.

ACKNOWLEDGEMENTS

The authors are extremely grateful to both reviewers for their comments which have served to clarify and improve the article.

REFERENCES

[1] Von Kármán, T: Überläminare und turbulence reibung. Z. Angew. Math. Mech. 1, 233–252 (1921).

[2] Schlichting, H., Gersten, K.: Boundary-Layer Theory. 8th ed., MacGraw-Hill, New York (2004)

[3] Elliott, L.: Elastico-viscous flow near a rotating disk. Phys. Fluids 14(6), 1086–1090 (1971).

[4] Kale, D.D., Mashelkar, R.A., Ulbrecht, J.: Rotational viscoelastic laminar boundary layer flow around a rotating disc. Rheol. Acta., 14(7), 631–640 (1975).

[5] Lentini, M., Keller, H. B.: The von Kármán swirling flows. SIAM J. Appl. Maths 38, 52–64 (1980).

[6] Guha, A., Sengupta, S.: Analysis of von Kármán's swirling flow on a rotating disc in Bingham fluids. Physics of Fluids 28, 013601 (2016).

[7] Mehmood, A., Asif Ali, Takhar, H.S., Bég, O.A., Islam, M.N., Wilson, L.S.: Unsteady Von Kármán swirling flow: analytical study using the Homotopy Method. Int. J. Applied Mathematics and Mechanics, 6(2): 67 – 84, (2010).

[8] Bearon, R.N., Grünbaum, D.: Bioconvection in a stratified environment: Experiments and theory. Physics of Fluids, 18, 127102 (2006).

[9] Kessler, J.O.: The external dynamics of swimming micro-organisms, in Progress in Phycological Research, Vol. 4, edited by F. E. Round and D. J. Chapman (Biopress, Bristol, 1986), 257–307.

[10] Plesset, M. S., Whipple, C. G., Winet, H.: Analysis of the steady state of the bioconvection in swarms of swimming microorganisms, in: Swimming and Flying in Nature, Vol. 1 (T. Y-T. Wu, C. J. Brokaw, and C. Brennan, eds.), pp. 339 – 360, Plenum Press, New York (1975).

[11] Manela, A., Frankel, I.: Generalized Taylor dispersion in suspensions of gyrotactic swimming micro-organisms. J. Fluid Mech.,490, 99 (2003).

[12] Vincent, R.V., Hill, N.A.: Bioconvection in a suspension of phototactic algae. J. Fluid Mech., 327, 343 (1996).

[13] Bearon, R.N.: An extension of generalized Taylor dispersion in unbounded homogeneous shear flows to run-and-tumble chemotactic bacteria. Phys. Fluids, 15, 1552 (2003).

[14] Bean, B.: Microbial Geotaxis. In: Colombetti G., Lenci F. (eds) Membranes and Sensory Transduction. Springer, Boston, MA, USA (1984).

[15] Nowakowska, G., Grgbecki, A.: On the mechanism of orientation of Paramecium caudatumin the gravity field. II. Contributions to a hydrodynamic model of geotaxis. Acta Protozool. 16, 359 – 376 (1977).

[16] Hershberger, P.K., Rensel, J.E., Matter, A.L., Taub, F.B.: Vertical distribution of the chloromonad flagellate Heterosigmacarterae in columns: implications for bloom development. Can. J. Fish. Aquat. Sci.0706-652X 54, 2228 (1997).

[17] Mormino, R., Bungay, H.R.: Compositions of bacterial cellulose and paper made with a rotating disk bioreactor. App. MicrobiolBiotechnol 62, 503-506 (2003).

[18] Lin, S.P., et al., Semi-continuous bacterial cellulose production in a rotating disk bioreactor and its materials properties analysis. Cellulose 21, 835–844 (2014).

[19] Kim, Y.J., Kim, J.N., Wee, Y.J., Park, D.H., Ryu, H.W.: Bacterial cellulose production by Gluconacetobacter sp. RKY5 in a rotary biofilm contactor. ApplBiochem Biotechnol. 48, 529–537 (2007).

[20] Magnacca, G., et al.: Refuse derived bio-organics and immobilized soybean peroxidase for green chemical technology. Process Biochemistry 47, 2025-2031 (2012).

[21] Sarkar, S., et al.: Production of a potentially novel antimicrobial compound by a biofilm-forming marine Streptomyces sp. in a niche-mimic rotating disk bioreactor. Bioprocess and Biosystems Engineering 33, 207–217 (2010).

[22]Sakurai, A., Hiroshi, I., Yoshiyuki, T., Mikio, S.: Simulation of citric acid production by rotating disk contactor. BiotechnolBioeng. 56, 689–696 (1997).

[23] Chtiouiet, O., et al.: Rotating discs bioreactor, a new tool for lipopeptides production. Process Biochemistry 47, 2020-2024 (2012).

[24] Qian, P.Y., Lau, S.C.K., Dahms, H.U., Dobretsov, S., Harder, T.: Marine biofilms as mediators of colonization by marine macro-organisms: implications for antifouling and aquaculture. Mar Biotechnol. 9, 399–410 (2007).

[25] Nikolov, L., Karamanev, D., Mamatarkova, V., Mehochev, D., Dimitrov, D.: Properties of the biofilm of Thiobacillus ferrooxidans formed in rotating biological contactor. Biochem Eng. J. 12, 43–48 (2002).

[26] Ekins-Coward, T., et al.: A microalgae biocomposite-integrated spinning disk bioreactor (SDBR): toward a scalable engineering approach for bioprocess intensification in light-driven CO2 absorption applications. Ind. Eng. Chem. Res. 58, 5936–5949 (2019).

[27] Hughes, W.F., Young, F.J.: The Electromagnetodynamics of Fluids. John Wiley, New York, USA (1966).

[28]Gregory, T.S., Schmidt, E.J., Zhang, S.H., Kwong, R.Y., Stevenson, W.G., Oshinski. J., et al.: Rapid quantification of stroke volume using magnetohydrodynamic voltages in 3T MRI: a feasibility study. Journal of Cardiovascular Magnetic Resonance 17, 32-40 (2015).

[29] Stan Gregory, T., et al.: The magnetohydrodynamic effect and its associated material designs for biomedical applications: a state-of-the-art review. Adv. Funct. Materials 26, 3942-3952 (2016).

[30] Wang, L.S., Flanagan, L., Monuki, E., Jeon, N.L., Lee, A.P.: A magnetohydrodynamic (MHD) microfluidic platform for cell switching. 3rd IEEE/EMBS Special Topic Conference on Microtechnology in Medicine and Biology; May, Oahu, Hawaii, USA (2005).

[31] Kósa, G., Jakab, P., Jólesz, F., Hata, N.: Swimming capsule endoscope using static and RF magnetic field of MRI for propulsion. IEEE International Conference on Robotics and Automation, ICRA 2008, Caltech,Pasadena, California, May 19-23, USA (2008).

[32] Oster, J., Llinares, R., Payne, S., Tse, Z.T.H., Schmidt, E.J., Clifford, G.D.: Comparison of three artificial models of the magnetohydrodynamic effect on the electrocardiogram. Computer Methods Biomechanics Biomedical Engineering 18, 1400–1417 (2015).

[33] Frauenrath, T., Fuchs, K., Dieringer, M., Ozerdem, C., Patel, N., Renz, W., et al.: Detailing the use of magnetohydrodynamic effects for synchronization of MRI with the cardiac cycle: a feasibility study. Journal of Magnetic Resonance Imaging. 36, 364–372 (2012).

[34] Ali, N., Asghar, Z., Sajid, M., Bég, O.A.: Biological interactions between Carreau fluid and micro-swimmers in a complex wavy canal with MHD effects. J. Brazilian Soc. Mech. Sci. Eng. 041:446(2019)) DOI.ORG/10.1007/s40430-019-1953-y (13 pages)

[35] Vasu, B., Dubey, A., Bég, O.A.: Finite element analysis of non-Newtonian magneto-hemodynamic flow conveying nanoparticles through a stenosed coronary artery. Heat Transfer-Asian Research (2019). DOI: 10.1002/htj.21598 (34 pages)

[36] Asghar, Z., Ali, N., Sajidand, M., Bég, O.A.: Micro-organism swimming propulsion through a shear rate-dependent biorheological fluid in an active channel assisted by a magnetic field. J. Magnetism and Magnetic Materials (2019). doi.org/10.1016/j.jmmm.2019.165283 (13 pages)

[37] Ali Abbas, M., Bég, O.A., Zeeshan, A., Hobiny, A., Bhatti, M.M.: Parametric analysis and minimization of entropy generation in bioinspired magnetized non-Newtonian nanofluid pumping using artificial neural networks and particle swarm optimization. Thermal Science and Engineering Progress (2021). doi.org/10.1016/j.tsep.2021.100930 (10 pages)

[38] Mallikarjuna, B., Gopi Krishna, G., Srinivas, J., Bég, O.A., Ali Kadir: Spectral numerical study of entropy generation in magneto-convective viscoelastic flow through a deformable porous medium with thermal radiation and buoyancy effects. ASME J. Thermal Science and Engineering Applications (2021).36 pages. doi.org/10.1115/1.4050935

[39] Castro, N., et al.: Magnetic bioreactor for magneto-mechano and electroactive tissue engineering strategies. Sensors, 20(12): 3340. 13 pages (2020).

[40] Choi, S.U.S.: Enhancing thermal conductivity of fluids with nanoparticles, The Proceedings of the 1995. ASME International Mechanical Engineering Congress and Exposition, San Francisco, USA, ASME 1995: 99–105.

[41] Bég, O.A.: Nonlinear multi-physical laminar nanofluid bioconvection flows: Models and computation, A. Sohail, Z. Li (Eds.): Computational Approaches in Biomedical Nano-Engineering, Wiley, Chapter 5, pp. 113-145 (2018).

[42] Chae, D., Degond, P., Liu, J.G.: Well-posedness for Hall-magnetohydrodynamics. Ann. Inst. H. Poincare Anal. Non-Lineaire 31, 555–565 (2014).

[43] Bég, O.A., Lik Sim, Zueco, J., Bhargava, R.: Numerical study of magnetohydrodynamic viscous plasma flow in rotating porous media with Hall currents and inclined magnetic field influence. Communications in Nonlinear Science and Numerical Simulation 15, 345-359 (2010).

[44] Khan, N. S., et al. Hall current and thermophoresis effects on magnetohydrodynamic mixed convective heat and mass transfer thin film flow. J. Phys. Commun. 3, 035009 (2019).

[45] Bég, O.A., Bég, T.A., Ferdows, M., Vasu, B., Ali Kadir, Leonard H.J., Kuharat, S.: Unsteady nonlinear magnetohydrodynamic micropolar transport phenomena with Hall and ion-slip current effects: numerical study. Int. J. Applied Electromagnetics & Mechanics, 1-33 (2020). DOI 10.3233/JAE-201508 (33 pages).

[46] Khan, N. S., Gul, T., Islam, S., Khan, A., Shah, Z.: Brownian motion and thermophoresis effects on MHD mixed convective thin film second-grade nanofluid flow with Hall effect and heat transfer past a stretching sheet. J. Nanofluids, 6(5), 812–829 (2017).

[47] Gaber, M., Mohamed, M.A.A.: The effects of radiation and Hall current on the unsteady MHD laminar convective fluid flow through porous medium due to a porous rotating disk. Int. J. Theor. Appl. Multiscale Mech. 4, (2009)

[48] Aboul-Hassan, A.L., Attia, H.A.: Flow due to a rotating disk with Hall effect. Physics Letters A 228, 286-290 (1997).

[49] Mustafa, I., et al.: Heat transfer in MHD stagnation point flow of a ferrofluid over a stretchable rotating disk. Journal of Molecular Liquids 219, 526-532 (2016).

[50] Thomas, C., Davies, C.: Global stability of the rotating-disc boundary layer with an axial magnetic field. J. Fluid Mech. 724, 510–526 (2013).

[51] Bég, O.A., Zueco, J., López-Ochoa, L.M.: Network numerical analysis of optically-thick hydromagnetic slip flow from a porous spinning disk with radiation flux, variable thermophysical properties and surface injection effects. Chemical Engineering Communications 198, 3, 360-384 (2011).

[52] Bég, O.A., Kabir, N., Uddin, M.J., Ismail, A.I.M., Alginah, Y.: Numerical investigation of Von Karman swirling bioconvective nanofluid transport from a rotating disk in a porous medium with Stefan blowing and anisotropic slip effects. Proc. IMechE- Part C- J. Mechanical Engineering Science(2020).DOI: 10.1177/0954406220973061 (19 pages).

[53] Yoo, Y.K.: Chemical Engineering Computation with MATLAB, CRC Press, USA (2016).

[54] Adomian, G.: Solving Frontier problems of Physics: The decomposition method. Kluwer Academic Publishers, USA (1994).

[55] Cramer, K.R., Pai, S.I.: Magnetofluid Dynamics for Engineers and Applied Physicists, MacGraw-Hill, New York, USA (1973).

[56] Fang, T.: Flow and mass transfer for an unsteady stagnation-point flow over a moving wall considering blowing effects. ASME J. Fluids Eng 136(7), 071103 (May 06, 2014) (7 pages) Paper No: FE-13-1342; doi: 10.1115/1.4026665.

[57] Umavathi, J.C., Sheremet, M.A.: Mixed convection flow of an electrically conducting fluid in a vertical channel using Robin boundary conditions with heat source/sink. European Journal of Mechanics B/Fluids 55, 132–145 (2016).

[58] Ferdows, M., Alsenafi, A., Bég, O.A., Bég, T.A., Ali Kadir: Numerical study of nano-biofilm stagnation flow from a nonlinear stretching/ shrinking surface with variable nanofluid and bio-convection transport properties. Scientific Reports (2021).11:9877 doi.org/10.1038/s41598-021-88935-9 (21 pages)

[59] Bég, O.A., Tripathi, D., Sochiand, T., Gupta, P.K.: Adomian decomposition method (ADM) simulation of magneto-biotribological squeeze film with magnetic induction effects. J. Mechanics Medicine Biology 15, 1550072.1-1550072.23 (2015).

[60] Bég, O.A., Mabood, F., Nazrul Islam, M.: Homotopy simulation of nonlinear unsteady rotating nanofluid flow from a spinning body Int. J. Engineering Mathematics 15, 2015, Article ID 272079, 15 pages (2015).

[61] Manzoor, N., Maqbool, K., Bég, O.A., Shaheen, S.: Adomian decomposition solution for propulsion of dissipative magnetic Jeffrey biofluid in a ciliated channel containing a porous medium with forced convection heat transfer. Heat Transfer - Asian Research (2018). DOI: 10.1002/htj.21394 (26 pages)

[62]Foster, K.R., Schwan, H.P. In: CRC Handbook of Biological Effects of Electromagnetic Fields. Part I. Polk C, Postow E, editors. Boca Raton, FL: CRC (1986).

[63] Kuure-Kinsey, M., et al.: Modeling and control of a rotating disk bioreactor, American Control Conference. Portland, Oregon, USA, June 8-10 (2005).

[64] Roy, A.K., Bég, O.A., Saha, A.K., Ramana Murthy, J.V.: Taylor dispersion in non-Darcy porous media with bulk chemical reaction: a model for drug transport in impeded blood vessels. J. Engineering Mathematics, 127:24 (18 pages) (2021).

[65] Das, S.K., Choi, S.U.S., Yu, W., Pradeep, T.: Nanofluids: Science and Technology, John Wiley & Sons, New Jersey, USA (2007).

[66] Lawrence, B.E., et al.: Flow dynamics in bioreactors containing tissue engineering scaffolds. Biotech. & Bioeng., 102, 935-947 (2009).

[67] Chandrawat, R.K., Joshi and, V., Bég, O.A.: Ion slip and Hall effects on generalized time-dependent hydromagnetic Couette flow of immiscible micropolar and dusty micropolar fluids with heat transfer and dissipation: a numerical study. J. Nanofluids, 10 (3), 431-446 (2021).